Journal of 先进陶瓷 ISSN 2226-4108 CN 10-1154/TQ Advanced Ceramics 清华大学出版社 Tsinghua University Press SciOpen

J Adv Ceram 2026, **15**: 9221330

https://doi.org/10.26599/JAC.2026.9221330

Research Article

Insight into the synergistic effect of rare-earth elements on the CMAS corrosion behavior in $(RE_{1/4}Tm_{1/4}Yb_{1/4}Lu_{1/4})_2Si_2O_7$ (RE = Gd, Ho and Sc) materials at 1300 °C

Ziyu Wang[1,2], Luchao Sun[1,✉], Tiefeng Du[1], Sikai Wang[1,2], Cui Zhou[3], Yixiu Luo[1], Jiemin Wang[1], Jingyang Wang[3,✉]

[1] *Shenyang National Laboratory for Materials Science, Institute of Metal Research, Chinese Academy of Sciences, Shenyang 110016, China.*

[2] *School of Materials Science and Engineering, University of Science and Technology of China, Shenyang 110016, China.*

[3] *Institute of Coating Technology for Hydrogen Gas Turbines, Liaoning Academy of Materials, Shenyang 110167, China.*

✉ Corresponding author.

E-mail: L. Sun, lcsun@imr.ac.cn;

J. Wang, jywang@imr.ac.cn

Received: March 23, 2026; Revised: May 11, 2026; Accepted: June 2, 2026

清華大學出版社 Tsinghua University Press | SciOpen

Abstract: Developing environmental barrier coating (EBC) materials with superior CMAS corrosion resistance represents a current research priority in rare-earth silicates. Previous studies have demonstrated that multicomponent rare-earth design can significantly enhance CMAS resistance performance, driven by differential rare-earth behavior during the corrosion process. This study investigates RE element synergy mechanisms in disilicates. We designed three multicomponent $(RE_{1/4}Tm_{1/4}Yb_{1/4}Lu_{1/4})_2Si_2O_7$ (RE = Gd, Ho and Sc) materials and subjected them to CMAS corrosion at 1300 °C for durations of 1, 4, and 50 h to elucidate the synergistic mechanisms of multicomponent rare-earth elements on CMAS corrosion. We systematically analyzed the role of rare-earth cations in CMAS corrosion by examining their influence on evolution of reactants and products. Results reveal that performance divergence in corrosion primarily stems from a mechanistic transition, from dissolution-reprecipitation to intergranular penetration, dictated by rare-earth ionic characteristics (mainly the cation radius). Comparative analysis confirms that an optimal active/inert stoichiometric ratio could simultaneously stimulate the precipitation-induced corrosion mitigation and the intrinsic resistance enhancement, establishing a design framework for multicomponent rare-earth disilicates for anti-CMAS EBC applications.

Keywords: Environmental barrier coating (EBC), rare-earth disilicate, multicomponent, CMAS corrosion

1 Introduction

Silicon carbide fiber-reinforced silicon carbide (SiC_f/SiC) ceramic matrix composites (CMCs) are recognized as highly promising for high-temperature structural applications in aero-engines, due to their high temperature capability, low density and high specific strength, etc [1,2]. However, in practical combustion environments, SiC_f/SiC CMCs encounter numerous challenges, including foreign object damage (FOD) [3], molten salt corrosion [4], water vapor corrosion [5] and molten calcium-magnesium-aluminosilicate (CMAS) corrosion [6]. The mechanical damage and chemical corrosion resulting from these challenges compromise the surface integrity of CMCs and accelerate material degradation, potentially leading to component failure. Consequently, environmental barrier coatings (EBCs) are employed to protect CMCs against premature failure [7–9].

Rare-earth disilicates $RE_2Si_2O_7$ (REDS), have been widely acknowledged as state-of-the-art environmental barrier coating material in commercial applications due to its superior thermochemical stability and high temperature water vapor corrosion resistance [9–13]. A primary limitation of $RE_2Si_2O_7$ EBCs for high-performance aero-engine applications-particularly at sustained operating temperatures exceeding 1300 °C is their inadequate resistance to CMAS deposits. These deposits, composed primarily of CaO, MgO, $AlO_{1.5}$, SiO_2 and traces of FeO_x, NiO and TiO_2 etc., are derived from the dust and debris ingested during engine operation. At temperatures exceeding 1200 °C, they undergo complete liquefaction and chemically interact with $RE_2Si_2O_7$ EBCs [14–19]. Extensive research has demonstrated that deposition significantly accelerates the degradation of $RE_2Si_2O_7$ EBCs through two primary mechanisms: (1) chemical reactions that progressively consume the coating material, and (2) intergranular penetration of molten CMAS along EBC grain boundaries, resulting in the failure of coating protective capability [13,20–28]. For instance, Zhao et al. [13] investigated the reactions between atmospheric plasma spray (APS) deposited $Yb_2Si_2O_7$ EBC and molten CMAS at 1300 °C, finding that reactions resulted in rapid dissolution of $Yb_2Si_2O_7$ and the precipitation of apatite with a composition approaching $Ca_2Yb_8(SiO_4)_6O_2$. Turcer et al. [22,23] systematically compared the

CMAS corrosion behaviors of γ-$Y_2Si_2O_7$, β-$Yb_2Si_2O_7$ and β-$Sc_2Si_2O_7$ with CMAS at 1500 °C. Their results revealed distinct degradation mechanisms: γ-$Y_2Si_2O_7$ underwent corrosion-induced phase transformation, forming a Y-Ca-Si apatite phase; whereas for both β-$Yb_2Si_2O_7$ and β-$Sc_2Si_2O_7$, CMAS melt penetrated along the grain boundaries with limited reaction-crystallization $Ca_2Yb_8(SiO_4)_6O_2$ in the case of β-$Yb_2Si_2O_7$. Moreover, subsequent studies on corrosion mechanism revealed that these two degradation behaviors may be correlated with the specific rare-earth ionic species present in the silicates and their influence on the formation of reaction products during corrosion [27,29]. To be specific, disilicates containing smaller RE cations (e.g. Yb^{3+} and Lu^{3+}) exhibit a reduced tendency of apatite formation and mainly suffered from grain boundary penetration [23,30]; while disilicates with larger RE cations (e.g. Y^{3+} and Gd^{3+}) incline to react with CAMS and promote the formation of apatite products [26–28]. From the perspective of the corrosive reaction, rare-earth elements with smaller cation sizes are considered to remain within the disilicate lattice, whereas those with larger cation sizes tend to actively diffuse into the CMAS melt to promote chemical reactions. Therefore, these two types of rare-earth elements can be classified as inert and active elements, respectively. These findings suggest that deliberately tuning the rare-earth ionic species, specifically adjusting the stoichiometric ratio of active and inert rare-earth elements via appropriate pathways, can offer a potential breakthrough in CMAS corrosion resistance by modulating the corrosion mechanism.

The recent advent of high-entropy or multicomponent design in materials engineering has made this concept significantly more feasible. To date, high-entropy/ multicomponent design has demonstrated significant advances in optimizing multiple properties of rare-earth disilicate environmental barrier coatings, including phase stability [31–36], thermal properties [37,38], and water vapor corrosion resistance abilities [39–43]. For the optimization of CMAS corrosion resistance of EBC, extensive research efforts have been devoted and numerous novel RE-disilicates with improved CMAS corrosion resistance have been developed. The underlying mechanisms for enhanced property are attributed to several possible reasons, such as sluggish atomic diffusion effect introduced

by high-entropy [37,44], enhanced bond energy in disilicate [45,46], and synergistic effects generated by multiple rare-earth cations [47,48]. In fact, all of these originate from the introduction of various rare-earth ions and their respective advantages in coupling [49,50]. For instance, the previous studies of $(Er_{1/4}Tm_{1/4}Yb_{1/4}Lu_{1/4})_2Si_2O_7$ [47,48] demonstrated that RE elements Er and Tm act as sacrificial elements, actively modifying the CMAS composition and effectively reducing its corrosion capacity, whereas Yb and Lu contribute to stabilizing the disilicates phase. These synergistic effects can inhibit the material recession of $(Er_{1/4}Tm_{1/4}Yb_{1/4}Lu_{1/4})_2Si_2O_7$ even when exposed to extreme conditions at 1500 °C. In addition, the beneficial effects of synergistic effects have also been demonstrated in other high entropy material systems, such as rare-earth zirconates [51,52] and rare-earth monosilicates [53,54]. Similar to other EBC materials [55,56], some studies have investigated the beneficial effects of corrosion products when RE disilicates subjected to CMAS corrosion. For instance, Wei et al. [57] designed four types of $(5RE_{1/5})_2Si_2O_7$, which mitigated excessive CMAS penetration by forming continuous cyclosilicate product layers. A similar mitigative effect was also observed by Dong et al. [58] in $(Yb_{1/5}Y_{1/5}Lu_{1/5}Sc_{1/5}Gd_{1/5})_2Si_2O_7$. Turcer et al. [59] established a protective apatite product layer between CMAS glass and REDS by increasing the Y content in $(Y_xYb_{1-x})_2Si_2O_7$ gradually. Chen et al. [60] further demonstrated that the RE elements with larger ionic radius (e.g. Y, Ho and Er) can facilitate the formation of a dense apatite array, thereby enhancing the protective effect of the entire corrosion product layer. Besides, the beneficial effects of the corrosion product layer in preventing further CMAS corrosion have been validated in $(Sc_{1/5}Nd_{1/5}Er_{1/5}Yb_{1/5}Lu_{1/5})_2Si_2O_7$ and $(Dy_{1/4}Ho_{1/4}Tm_{1/4}Yb_{1/4})_2Si_2O_7$ by Ridley et al. [61], Zhang et al. [62], Wang et al. [63] , and Abrar et al. [64] respectively and have also been established as an important corrosion mitigation strategy in the reviews of Qian et al. [65] and Chen et al. [66].

Building on the above findings, it can be concluded that the CMAS corrosion resistance of multicomponent rare-earth disilicates $(xRE_{1/x})_2Si_2O_7$ can be enhanced by controlled corrosion reactions and accelerated formation of dense corrosion products. These two processes can be inspired

synergistically via proper selection of functional RE components in $(xRE_{1/x})_2Si_2O_7$ EBCs. Accordingly, extending the previous work on $(Er_{1/4}Tm_{1/4}Yb_{1/4}Lu_{1/4})_2Si_2O_7$ [47,48], we designed three new $(RE_{1/4}Tm_{1/4}Yb_{1/4}Lu_{1/4})_2Si_2O_7$ (RE = Gd, Ho and Sc) with distinct ionic radius, abbreviated as GTYL, HTYL and STYL. The element selection is guided by the following considerations: Firstly, component selection is constrained by the rare-earth disilicate structural stability criterion established in our prior work [31]. Secondly, as mentioned earlier, the CMAS corrosion behaviors of disilicate exhibit a close relationship to the componential cationic size. Thus, the substitute rare-earth species for Er should have a larger or smaller radius. Considering that the $(Er_{1/4}Tm_{1/4}Yb_{1/4}Lu_{1/4})_2Si_2O_7$ formed by the last four rare-earth elements represents the maximum limit of the minimum average cationic radius $(xRE_{1/x})_2Si_2O_7$ that lanthanides can reach, it is necessary to introduce rare-earth elements from other periods to achieve further reduction. Coincidentally, due to the absence of 4p, 4d and 4f electron shells, Sc exhibits the smallest cationic radius (0.745 Å) and undoubtedly becomes the most suitable choice. Meanwhile, in order to synthesize $(xRE_{1/x})_2Si_2O_7$ with a larger average cationic radius compared with $(Er_{1/4}Tm_{1/4}Yb_{1/4}Lu_{1/4})_2Si_2O_7$, Ho (0.901 Å) even Gd (0.938 Å) were selected as the representatives of heavy and light rare-earth elements, respectively. Notably, although Y is also a non-lanthanide element and has been considered as a promising alternative [22,67,68], it is still excluded due to the highly similar cationic radius (0.900 Å) to that of Ho (0.901 Å). Therefore, the finally designed materials are $(RE_{1/4}Tm_{1/4}Yb_{1/4}Lu_{1/4})_2Si_2O_7$ (RE=Gd, Ho and Sc), abbreviated as GTYL, HTYL and STYL, to enable a comparative investigation of the influence from the rare earth elements on the CMAS corrosion process. Subsequently, the CMAS corrosion experiments were conducted on these materials at 1300 °C for durations of 1, 4, and 50 h (denoted as CMAS-1 h, CMAS-4 h and CMAS-50 h, respectively). By analyzing the influences of RE species on CMAS corrosion process and resultant products exhibited by these $(4RE_{1/4})_2Si_2O_7$, we elucidated the distinct performance characteristics of the compared rare-earth species during CMAS corrosion, specifically their active facilitation of precipitation versus passive corrosion resistance. This mechanistic understanding enabled the proposal of material design

principles for activating synergistic effects in multicomponent rare-earth disilicates.

2 Experimental Procedure

The bulk samples of $(Gd_{1/4}Tm_{1/4}Yb_{1/4}Lu_{1/4})_2Si_2O_7$ and $(Ho_{1/4}Tm_{1/4}Yb_{1/4}Lu_{1/4})_2Si_2O_7$ were prepared through conventional sintering of their corresponding precursor powders, while $(Sc_{1/4}Tm_{1/4}Yb_{1/4}Lu_{1/4})_2Si_2O_7$ bulk material was fabricated via solid-state reaction using stoichiometric mixtures of $(Sc_{1/4}Tm_{1/4}Yb_{1/4}Lu_{1/4})_2SiO_5$ and SiO_2 as starting reagents. The unique process of $(Sc_{1/4}Tm_{1/4}Yb_{1/4}Lu_{1/4})_2Si_2O_7$ bulk aims to facilitate the sintering of the grain boundaries by using the reaction heat of $RE_2SiO_5 + SiO_2 \rightarrow RE_2Si_2O_7$ during the subsequent hot-pressed process. Related details are provided in Fig. S1 and Note 1 in the Electronic Supplementary Material (ESM). For the synthesis of $(Gd_{1/4}Tm_{1/4}Yb_{1/4}Lu_{1/4})_2Si_2O_7$, $(Ho_{1/4}Tm_{1/4}Yb_{1/4}Lu_{1/4})_2Si_2O_7$ and $(Sc_{1/4}Tm_{1/4}Yb_{1/4}Lu_{1/4})_2SiO_5$ powders, commercially available RE_2O_3 (Rear-Chem. Hi-Tech. Co. Ltd., RE = Gd, Ho, Tm, Yb, Lu, and Sc) and SiO_2 (Sinopharm Chemical Reagent Co. Ltd.) powders were used as starting materials. Each RE_2O_3 and SiO_2 powder was weighed according to a molar ratio of 1:8 or 1:4 for $(4RE_{1/4})_2Si_2O_7$ and $(4RE_{1/4})_2SiO_5$, respectively. To account for potential SiO_2 volatilization during high-temperature processing and to ensure complete solid solution formation, all batches incorporated a 3 mol% excess of SiO_2 beyond the theoretical stoichiometry [45,69]. The weighed powders were mixed and ball-milled in silicon nitride jars with anhydrous ethanol as milling media at a speed of 275 rpm for 15 h. The obtained slurry was oven-dried at 60 °C for 24 hours, followed by sieving through a 120-mesh sieve to collect precursor particles. To initiate solid-state reactions, the precursor was subsequently calcined in a muffle furnace under ambient atmosphere at 1550 °C for 10 hours. Finally, for the fabrication of bulk materials, the obtained powders were loaded into a BN-coated graphite die with a diameter of 50 mm and hot-pressed under 30 MPa pressure at 1860 °C for 2 h in Ar atmosphere.

Prior to CMAS corrosion testing, $(Gd_{1/4}Tm_{1/4}Yb_{1/4}Lu_{1/4})_2Si_2O_7$, $(Ho_{1/4}Tm_{1/4}Yb_{1/4}Lu_{1/4})_2Si_2O_7$ and $(Sc_{1/4}Tm_{1/4}Yb_{1/4}Lu_{1/4})_2Si_2O_7$ bulks were cut into samples with 10×10×3 mm^3 using a diamond saw.

Both the top and bottom surfaces of these samples were polished, and two parallel grooves approximately 0.5 mm deep were cut on the top surface of the samples using a 0.05 mm thick saw blade. These two grooves were respectively machined at a distance of 1mm from the edges on both sides of the sample, and can help to define the reaction area and identify the original surface of the corroded specimens after CMAS corrosion test.

A typical CMAS powder composition, with molar ratio of 33CaO-9MgO-13$AlO_{1.5}$-45SiO_2 was adopted for subsequence experiments. Notably, it is based on the average of deposits on aircraft turboshaft shrouds operated in a desert environment [16,70], and has been widely employed as a standard corrosive medium in CMAS exposure experiments for several potential T/EBC materials systems, such as zirconates [71], tantalates [72], phosphates [73,74], and rare-earth oxides [75]. Stoichiometric amounts of CaO, MgO, Al_2O_3, and SiO_2 powders were mixed and milled with anhydrous ethanol for 15 h. The resulting mixture was dried and sieved. Then the powder mixture was subjected to pressure-less sintering in air at 1150 °C for 24 h with a heating rate of 5 °C/min. A suspension of the CMAS powder was prepared using anhydrous ethanol as the dispersant and then deposited dropwise onto the defined reaction area of the polished samples, and subsequently dried in an oven. This process was repeated until a CMAS loading of 30 mg/cm^2 was achieved. The CMAS-coated samples were then placed into a muffle furnace and heated to 1300 °C with holding time of 1 h, 4 h and 50 h, respectively.

Phase analysis of $(Gd_{1/4}Tm_{1/4}Yb_{1/4}Lu_{1/4})_2Si_2O_7$, $(Ho_{1/4}Tm_{1/4}Yb_{1/4}Lu_{1/4})_2Si_2O_7$ and $(Sc_{1/4}Tm_{1/4}Yb_{1/4}Lu_{1/4})_2Si_2O_7$ bulk materials and the surface of CMAS-corroded specimens were performed by an X-ray diffractometer (XRD; D/max-2400, Rigaku, Tokyo, Japan). Morphologies and elemental compositions of corroded samples were characterized through a scanning electron microscopy (SEM; Gemini 300, Zeiss, Germany), equipped with an energy dispersive X-ray spectrometer (EDS; Ultim max, Oxford Instruments, UK). Additionally, back-scattered electron (BSE) images were binarized, stitched and measured using the image processing software ImageJ. These

processes enabled the precise distinction of various phases and defects (e.g. pores, cracks, and grain boundaries) and further measurements of recession depth, reaction product layer thickness, grain aspect ratio (length to diameter ratio, L/D) and porosity in the corrosion product layers.

3 Results and discussion

3.1 Characterizations of bulk materials before CMAS corrosion

Figure 1 presents the X-ray diffraction (XRD) profiles of the fabricated $(Gd_{1/4}Tm_{1/4}Yb_{1/4}Lu_{1/4})_2Si_2O_7$ (GTYL), $(Ho_{1/4}Tm_{1/4}Yb_{1/4}Lu_{1/4})_2Si_2O_7$ (HTYL) and $(Sc_{1/4}Tm_{1/4}Yb_{1/4}Lu_{1/4})_2Si_2O_7$ (STYL) bulk materials. As revealed in Fig. 1(a), all diffraction patterns show remarkable consistency with the standard PDF cards, demonstrating the formation of single-phase solid solutions. What should be noted is that the GTYL phase exhibits diffraction peaks matching with γ-type $Er_2Si_2O_7$ (PDF #24-0062), indicating its crystallization in the monoclinic $P2_1/c$ structure. Conversely, both HTYL and STYL demonstrate peak profiles consistent with β-type $Yb_2Si_2O_7$ (PDF #25-1345), confirming their adoption of the monoclinic $C2/m$ space group symmetry. Furthermore, Figs. 1(b) and 1(c) present the enlarged views of characteristic diffraction peaks from Fig. 1(a). Specifically, the diffraction peaks (111), (021), and $(\bar{2}01)$ were selected for HTYL and STYL phases, whereas peaks (111), $(\bar{1}12)$, and (013) were selected for GTYL. As shown in Fig 1(b), the (111), (021), and $(\bar{2}01)$ peaks of HTYL demonstrate a noticeably shift toward lower diffraction angles when compared with $Yb_2Si_2O_7$ reference pattern (PDF #25-1345), while STYL exhibits an opposite peak-shifting tendency. These phenomena are primarily attributed to the lattice distortion induced by the incorporation of multi-component RE^{3+} ions, with the degree of distortion quantitatively characterized by the average cationic radius ($\bar{r}$) [60]. Computational results revealed the following $\bar{r}$ sequence: HTYL (0.878 Å) > $Yb_2Si_2O_7$ (0.868 Å) > STYL (0.839 Å). In accordance with Bragg's law, the lattice expansion in HTYL consequently led to peak shifting toward lower angles, whereas the lattice contraction in STYL induced an opposing shift direction. Furthermore, as illustrated in Fig. 1(c), the (111), $(\bar{1}12)$, and (013) diffraction peaks of GTYL show nearly identical positions with the reference

$Er_2Si_2O_7$ pattern (PDF #24-0062). This remarkable correspondence arises from the minimal difference between the average cationic radius between $\bar{r}_{(GTYL)}$=0.887 Å and $r_{(Er)}$=0.890 Å and provides compelling evidence for the successful formation of single-phase solid solution in GTYL.

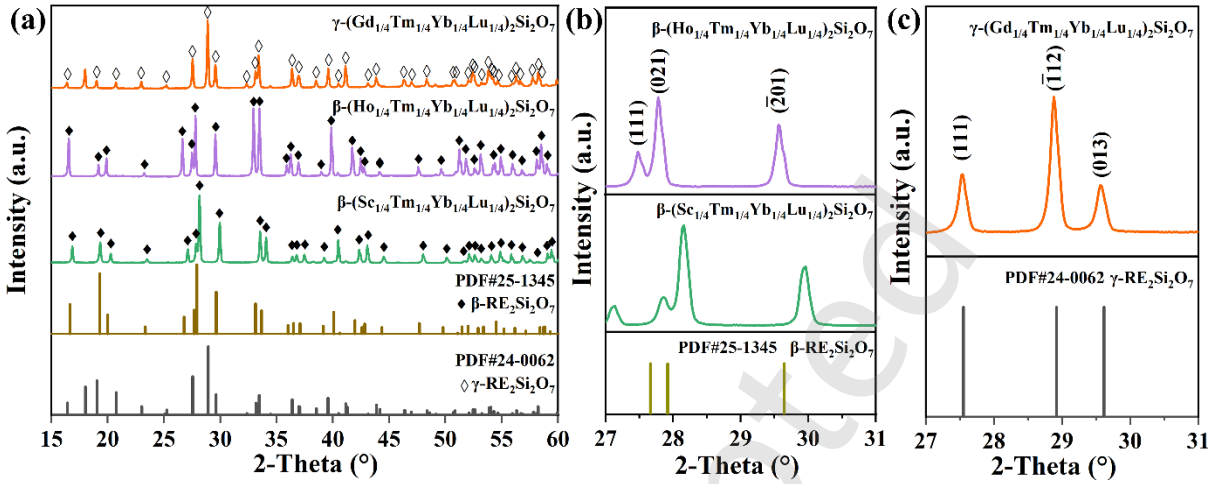

Fig. 1 The X-ray diffractometer (XRD) patterns of (a) three multicomponent rare-earth disilicate bulks and local patterns ranging from 27° to 31° for (b) $(Ho_{1/4}Tm_{1/4}Yb_{1/4}Lu_{1/4})_2Si_2O_7$, $(Sc_{1/4}Tm_{1/4}Yb_{1/4}Lu_{1/4})_2Si_2O_7$ and (c) $(Gd_{1/4}Tm_{1/4}Yb_{1/4}Lu_{1/4})_2Si_2O_7$.

Figure 2 presents the scanning electron microscopy (SEM) images and corresponding energy dispersive X-ray spectroscopy (EDS) elemental mapping results of the polishing surfaces of GTYL, HTYL and STYL, respectively. All examined surfaces are devoid of microstructural defects (e.g., pores or cracks), with only minor polishing traces in Figs. 2(a)-2(c), indicating the high density of the three bulk materials. Furthermore, EDS mapping results of all the three samples reveal uniformly distributed color pixels across the entire field of view, suggesting a homogeneous distribution of all RE elements in these $(4RE_{1/4})_2Si_2O_7$ bulks. EDS analysis of the cationic ratios within the regions in Fig. 2 was also conducted and the data was listed in Table 1. Notably, the relative proportions of the four rare-earth elements in these $(4RE_{1/4})_2Si_2O_7$ bulks remain generally consistent, further confirming that the stoichiometry is comparable to the ideal composition. Additionally, the combined RE-to-Si ratio consistently approximates 1:1 across all samples, confirming successful synthesis of the target $(4RE_{1/4})_2Si_2O_7$ materials.

Furthermore, a verification of the chemical composition consistency between the prepared CMAS

powder and the intended CMAS composition (33CaO-9MgO-13$AlO_{1.5}$-45SiO_2) was conducted using SEM-EDS analysis (see Fig. S2 and Table S1). The prepared CMAS powder shows a similar elemental composition (in mol%) ((31.52 ± 0.26) CaO- (10.12 ± 0.45) MgO- (14.60 ± 0.42) $AlO_{1.5}$- (43.76 ± 0.44) SiO_2, Ca/Si ≈ 0.72) to the intended value (33CaO-9MgO-13$AlO_{1.5}$-45SiO_2, Ca/Si ≈ 0.73). The related details are provided in Note 2 in the Electronic Supplementary Material (ESM).

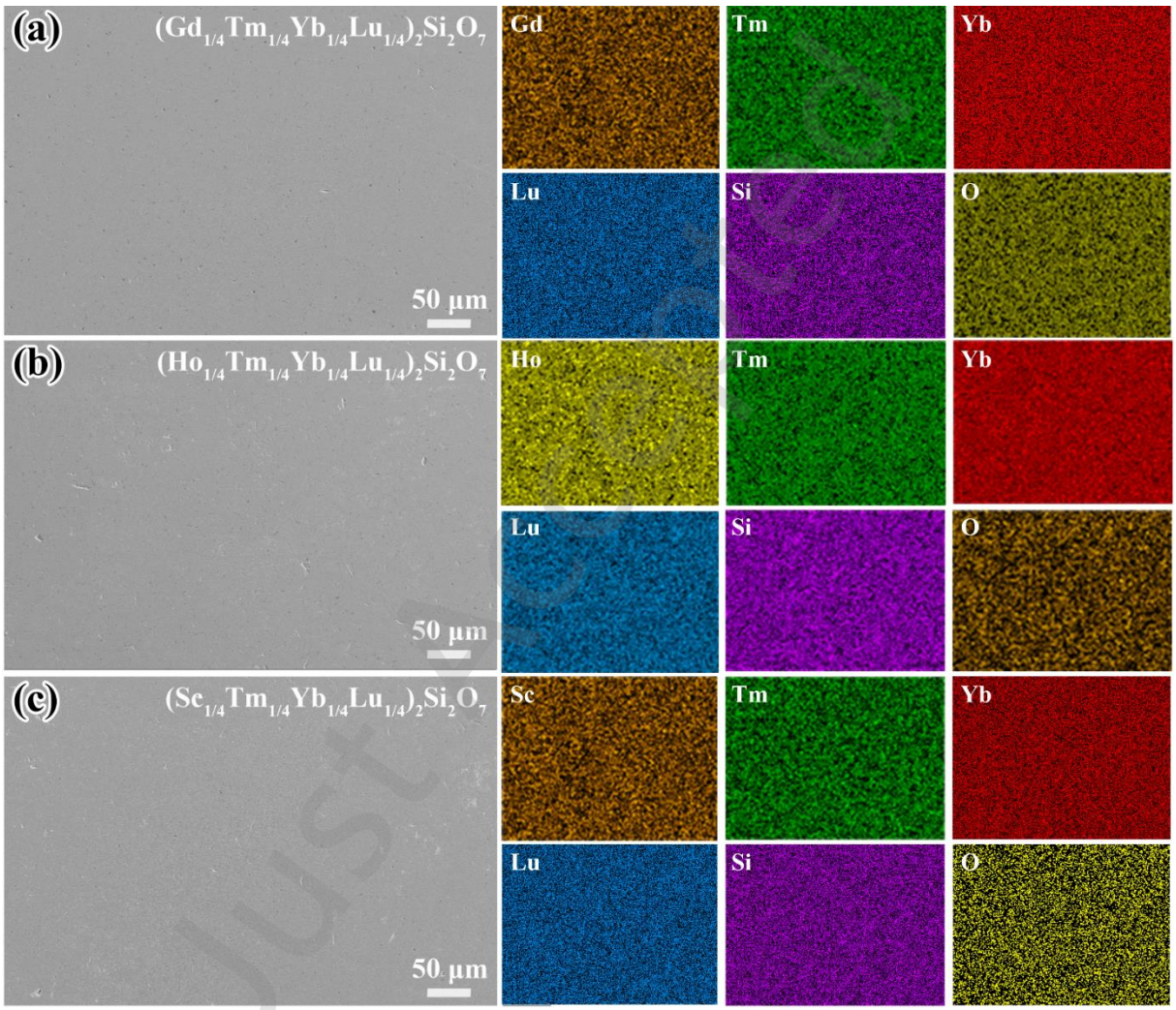

Fig. 2 Scanning electron microscopy (SEM) images of the surface and corresponding energy dispersive X-ray spectroscopy (EDS) elemental mapping results of (a) $(Gd_{1/4}Tm_{1/4}Yb_{1/4}Lu_{1/4})_2Si_2O_7$, (b) $(Ho_{1/4}Tm_{1/4}Yb_{1/4}Lu_{1/4})_2Si_2O_7$ and (c) $(Sc_{1/4}Tm_{1/4}Yb_{1/4}Lu_{1/4})_2Si_2O_7$ bulks.

Table 1 Elemental compositions (in mol%, obtained from SEM-EDS data) of $(Gd_{1/4}Tm_{1/4}Yb_{1/4}Lu_{1/4})_2Si_2O_7$, $(Ho_{1/4}Tm_{1/4}Yb_{1/4}Lu_{1/4})_2Si_2O_7$ and $(Sc_{1/4}Tm_{1/4}Yb_{1/4}Lu_{1/4})_2Si_2O_7$ in Fig. 2.

Composition	Si	RE^I	Tm	Yb	Lu
RE^I=Gd	51.68 ± 0.86	11.57 ± 0.32	11.62 ± 0.99	11.89 ± 0.41	13.25 ± 1.24
RE^I=Ho	50.60 ± 0.60	12.40 ± 0.21	11.52 ± 0.30	12.90 ± 0.35	12.58 ± 0.43
RE^I=Sc	55.85 ± 0.32	11.65 ± 0.29	11.01 ± 0.24	11.18 ± 0.16	11.01 ± 0.11

3.2 Characterizations of samples after CMAS corrosion

Figure 3 presents the XRD results for the surfaces of three $(4RE_{1/4})_2Si_2O_7$ specimens after exposure to molten CMAS at 1300 °C for 1, 4, and 50 hours. It is seen that disilicate phases can be detected in all the specimens. Moreover, characteristic diffraction peaks of apatite-phases ($Ca_2RE_8(SiO_4)_6O_2$, PDF #27-1054) are clearly observed in $(Gd_{1/4}Tm_{1/4}Yb_{1/4}Lu_{1/4})_2Si_2O_7$ (Fig. 3(a)) and $(Ho_{1/4}Tm_{1/4}Yb_{1/4}Lu_{1/4})_2Si_2O_7$ (Fig. 3(b)) specimens. This phase has been widely recognized as a typical corrosion product formed during the interaction between rare-earth disilicates and CMAS [46,50,76]. To elucidate the characteristics of these apatite phases, key diffraction peaks were systematically compared. As shown in Fig. 3(a), the diffraction peaks corresponding to the (200) and (300) crystal planes of apatite phase exhibit higher intensities in GTYL-4 h, whereas those of the (002) and (004) planes are more pronounced in GTYL-1 h. The intensity variation of the (400) plane remains relatively minor across all GTYL specimens. As for HTYL (Fig. 3(b)), only the (004) plane of apatite demonstrates a time-dependent enhancement in peak intensity with prolonged corrosion duration. The other peaks of apatite phase exhibit no clear regularity. Besides, no distinct diffraction peaks corresponding to the apatite phase were observed on the corroded surface of $(Sc_{1/4}Tm_{1/4}Yb_{1/4}Lu_{1/4})_2Si_2O_7$ after CMAS corrosion. In addition to the crystalline phases, both Fig. 3(a) and Fig. 3(b) exhibit slight broad peaks centered at approximately 30°, indicating the presence of

amorphous phase in corroded $(Gd_{1/4}Tm_{1/4}Yb_{1/4}Lu_{1/4})_2Si_2O_7$ and $(Ho_{1/4}Tm_{1/4}Yb_{1/4}Lu_{1/4})_2Si_2O_7$ samples.

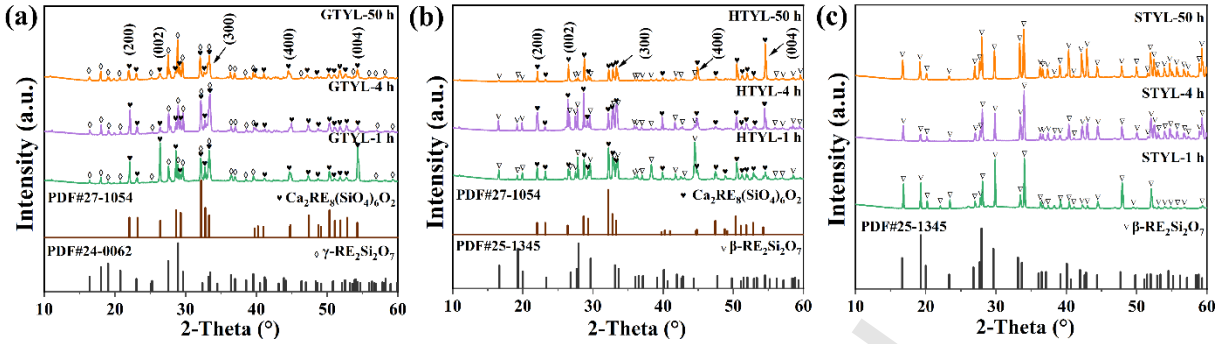

Fig. 3 XRD patterns of the surface of (a) $(Gd_{1/4}Tm_{1/4}Yb_{1/4}Lu_{1/4})_2Si_2O_7$, (b) $(Ho_{1/4}Tm_{1/4}Yb_{1/4}Lu_{1/4})_2Si_2O_7$ and (c) $(Sc_{1/4}Tm_{1/4}Yb_{1/4}Lu_{1/4})_2Si_2O_7$ corroded by CMAS melt at 1300 °C for 1, 4, and 50 hours.

Figure 4 illustrates the surface observations of the three $(4RE_{1/4})_2Si_2O_7$ after exposure to CMAS for different durations. As shown in Fig. 4(a), numerous rod-like phases are observed on the surface of the GTYL-1 h, embedded within a dark-grey background. Based on the elemental atomic ratio of point P1 in Table 2, these rod-like phases were identified as apatite phase ($Ca_2RE_8(SiO_4)_6O_2$). This identification is consistent with the corresponding diffraction peaks detected in Fig. 3(a). The extensively distributed dark-grey region (labeled as P2 in Fig. 4(a)), containing characteristic compositions of Ca, Mg, Al, Si, and RE elements, was confirmed to be the residual CMAS. What should be noted is that the presence of rare-earth elements (RE = Gd, Tm, Yb, and Lu) within the residual CMAS provides direct evidence of GTYL dissolution during high-temperature corrosion. Similar morphologies and phases can be observed in both GTYL-4 h (Fig. 4(b)) and GTYL-50 h (Fig. 4(c)). The differentiating aspect resides in the varying proportions of the reaction products. Notably, GTYL-4 h exhibits significantly fewer apatite grains compared to GTYL-1 h and GTYL -50 h. These observations are consistent with the lack of a clear correlation between the apatite diffraction peak intensity and the exposure time, as shown in Fig. 3(a). Furthermore, high-magnification BSE imaging of GTYL-50 h (Fig. 4(d)) reveals the coexistence of two distinct apatite morphologies within the CMAS glass matrix: the predominant rod-like phase and an additional block-like phase. The block-like phase (P3) exhibits a near-hexagonal morphology, as shown by the inset in Fig. 4(d), outlined by

the red dashed line. Quantitative EDS compositional analysis at point P3 (Table 2) confirms that this phase also corresponds to apatite phase ($Ca_2RE_8(SiO_4)_6O_2$), consistent with the previous report that rare-earth apatite phases exhibit a hexagonal prismatic structure [44,77]. That is to say, apatite phases exhibiting dual morphological features present on the surface of the CMAS-corroded GTYL-50 h sample: one characterized by horizontal growth, designated as "horizontal apatite", and the other by vertical growth, designated as "vertical apatite". Similar microstructural features have been widely observed in prior research [77–80]. For instance, Tian et al. [80] investigated the formation of horizontal apatite grains occurs in both reaction and cooling stages through an *in-situ* observation and found that the different morphologies and irregular quantities of horizontal apatite grains resulted from the two-stage precipitation process during CMAS corrosion. Figs. 4(e) and 4(f) illustrate that the corroded HTYL and GTYL have similar surface morphology in the initial four hours, especially the needle-like phase at P4 and the dark-grey background (P5). The corresponding EDS compositions in Table 2 confirmed that the specimen surfaces are composed of apatite and residual CMAS. Notably, HTYL-50 h exhibits a distinct surface morphology (Figs. 4(g) and 4(h)) compared to GTYL-50 h. High-magnification BSE imaging (Fig. 4h) reveals vertically aligned apatite grains (P6) densely covering the surface, with residual CMAS only existing in the interstices between densely distributed apatite grains. In contrast to $(Gd_{1/4}Tm_{1/4}Yb_{1/4}Lu_{1/4})_2Si_2O_7$ and $(Ho_{1/4}Tm_{1/4}Yb_{1/4}Lu_{1/4})_2Si_2O_7$, the corroded surface of $(Sc_{1/4}Tm_{1/4}Yb_{1/4}Lu_{1/4})_2Si_2O_7$ exhibited a distinct microstructure: rod-shaped apatite phases were scarcely observed, while the surface was predominantly covered by white-contrast short-rod (P8, Fig. 4(i)) and blocky grains (P9, Fig. 4(i)) embedded in dark-grey CMAS residues (P7, Fig. 4(i)). Through correlative analysis of EDS-derived RE/Si atomic ratios (~1:1, Table 2) and XRD peak assignments (Fig. 3(c)), these two white-contrast phases (P8 and P9) are identified as STYL grains. Similar microstructural features were observed on the surface of STYL-4 h (Fig. 4(j)). In addition, both low- and high-magnification surface analysis of STYL-50 h (Figs. 4(k) and 4(l)) reveals near-complete CMAS depletion, with the corrosion surface consisting exclusively of blocky grains.

EDS compositional analysis of representative grains (P10 in Table 2) confirms their identity as $(Sc_{1/4}Tm_{1/4}Yb_{1/4}Lu_{1/4})_2Si_2O_7$ rare-earth disilicates.

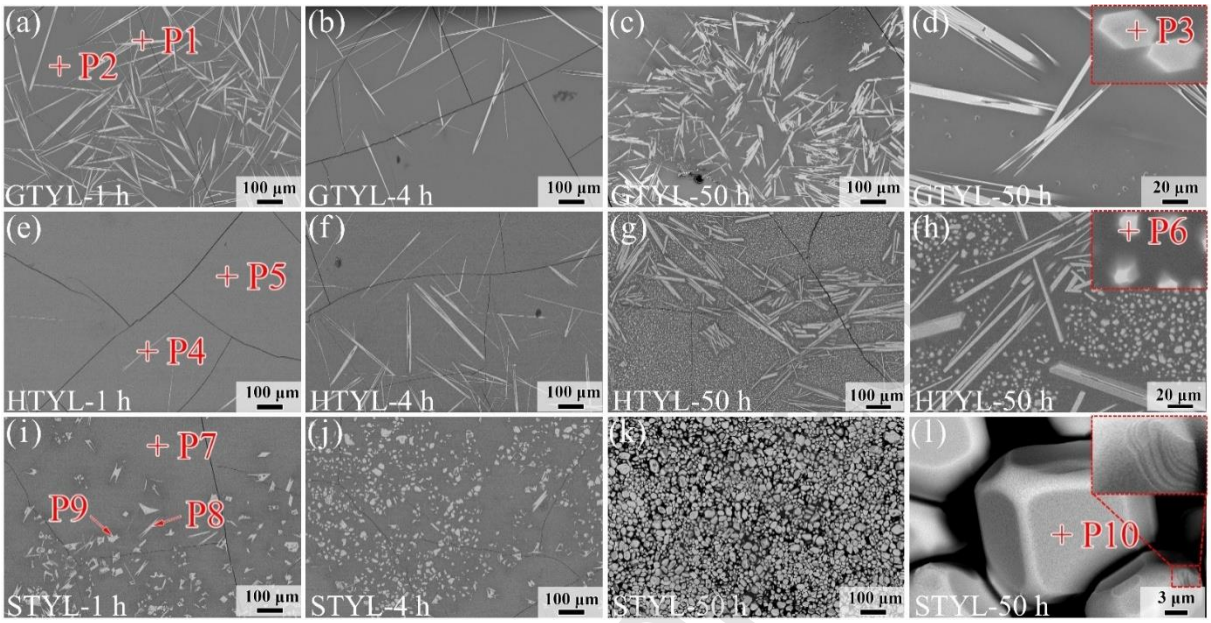

Fig. 4 Back-scattered electron (BSE) images of the specimen surface of (a-d) $(Gd_{1/4}Tm_{1/4}Yb_{1/4}Lu_{1/4})_2Si_2O_7$, (e-h) $(Ho_{1/4}Tm_{1/4}Yb_{1/4}Lu_{1/4})_2Si_2O_7$ and (i-l) $(Sc_{1/4}Tm_{1/4}Yb_{1/4}Lu_{1/4})_2Si_2O_7$ corroded by CMAS melt at 1300 °C for 1, 4 and 50 hours, (d), (h), and (l) are high magnification images of Figs. 4(c), 4(g) and 4(k), respectively.

Table 2 Elemental composition (in mol%, obtained from SEM-EDS data) from regions in Fig. 4 of three $(4RE_{1/4})_2Si_2O_7$ after CMAS corrosion at 1300 °C for 1 h, 4 h, and 50 h.

Point	CaO	MgO	$AlO_{1.5}$	SiO_2	$RE^IO_{1.5}$	$TmO_{1.5}$	$YbO_{1.5}$	$LuO_{1.5}$	Phase
P1 (RE^I=Gd)	14.31 ± 1.19	/	/	39.74 ± 0.77	12.89 ± 0.49	11.56 ± 0.55	11.34 ± 0.40	10.16 ± 0.42	Apatite
P2 (RE^I=Gd)	25.19 ± 0.26	6.97 ± 0.38	12.38 ± 1.09	47.90 ± 0.56	1.66 ± 0.10	1.94 ± 0.11	2.11 ± 0.20	1.85 ± 0.15	CMAS
P3 (RE^I=Gd)	12.65 ± 0.36	/	/	50.74 ± 1.00	11.26 ± 0.44	8.71 ± 0.31	8.83 ± 0.30	7.81 ± 0.28	Apatite
P4 (RE^I=Ho)	13.04 ± 0.48	/	/	38.18 ± 1.21	13.97 ± 0.52	12.54 ± 0.24	12.07 ± 0.56	10.20 ± 0.52	Apatite
P5 (RE^I=Ho)	26.09 ± 0.56	6.24 ± 0.35	10.56 ± 1.20	49.41 ± 0.66	1.97 ± 0.10	1.89 ± 0.09	2.13 ± 0.14	1.72 ± 0.24	CMAS
P6 (RE^I=Ho)	12.78 ± 0.40	/	/	38.80 ± 2.66	13.83 ± 0.86	12.28 ± 0.70	11.90 ± 0.61	10.41 ± 0.73	Apatite
P7 (RE^I=Sc)	26.42 ± 0.45	6.75 ± 0.44	11.67 ± 0.99	47.02 ± 0.37	2.19 ± 0.12	2.10 ± 0.17	2.16 ± 0.14	1.69 ± 0.19	CMAS
P8 (RE^I=Sc)	0.63 ± 0.32	/	/	51.23 ± 0.76	11.91 ± 0.60	10.88 ± 0.57	12.75 ± 0.49	12.59 ± 0.52	Disilicate
P9 (RE^I=Sc)	0.38 ± 0.18	/	/	51.24 ± 1.57	12.11 ± 0.82	10.64 ± 0.69	12.94 ± 0.76	12.68 ± 0.62	Disilicate
P10 (RE^I=Sc)	/	/	/	49.81 ± 0.85	12.00 ± 0.38	12.11 ± 0.40	13.04 ± 0.40	13.04 ± 0.24	Disilicate

To investigate the phase evolutions of $(Gd_{1/4}Tm_{1/4}Yb_{1/4}Lu_{1/4})_2Si_2O_7$, $(Ho_{1/4}Tm_{1/4}Yb_{1/4}Lu_{1/4})_2Si_2O_7$ and $(Sc_{1/4}Tm_{1/4}Yb_{1/4}Lu_{1/4})_2Si_2O_7$ under CMAS attack, phase morphologies and their elemental compositions in the cross-sections of samples at progressive corrosion stages (1, 4, and 50 h) were systematically examined through SEM-EDS analysis. The BSE-EDS analysis in Fig. 5(a) reveals three distinct zones in the cross-section of GTYL-1 h, delineated by two red dashed lines based on morphological and compositional contrasts. The topmost dark-contrast region, identified as residual CMAS glass through EDS analysis (P1 in Table 3), aligns with surface observations in Fig. 4(a). An intermediate continuous layer (between dashed lines) consisting of needle-like apatite-phase grains, confirmed as $Ca_2RE_8(SiO_4)_6O_2$ by stoichiometric analysis (P2 in Table 3). Beneath the apatite layer, the RE/Si ratio of P3 in Table 3 is comparable to that of $RE_2Si_2O_7$, indicating the area as uncorroded $(Gd_{1/4}Tm_{1/4}Yb_{1/4}Lu_{1/4})_2Si_2O_7$. In this study, we defined the upper surface of the uncorroded $(Gd_{1/4}Tm_{1/4}Yb_{1/4}Lu_{1/4})_2Si_2O_7$ material as the "corrosion front". Evidently, the continuous apatite layer constitutes the corrosion product resulting from the interaction of GTYL with CMAS. The detailed chemical reaction equation is widely acknowledged [29,67,76], as shown in Eq. 1:

$$4RE_2Si_2O_7 + 2CaO\ (CMAS) \rightarrow Ca_2RE_8(SiO_4)_6O_2 + 2SiO_2 \quad (1)$$

Additionally, a gray-contrast phase (labeled as P4 in Fig. 5(a)) emerges at the CMAS glass/apatite layer interface. Stoichiometric analysis of Ca, RE, and Si concentrations (P4 in Table 3) confirms this phase as $Ca_3RE_2(Si_3O_9)_2$. The chemical reaction equation for the formation of $Ca_3RE_2(Si_3O_9)_2$ with cyclosilicate structure has also been widely reported [57,81–83], which can be described by Eq. 2:

$$RE_2Si_2O_7 + 3CaO\ (CMAS) + 4SiO_2\ (CMAS) \rightarrow Ca_3RE_2(Si_3O_9)_2 \quad (2)$$

What should be mentioned is that the XRD pattern in Fig. 3(a) shows no detectable peaks corresponding to $Ca_3RE_2(Si_3O_9)_2$. This absence may be attributed to the low volumetric fraction of the cyclosilicate phase and possible signal shielding by the overlying CMAS glass layer.

Figure 5(b) shows the cross-sectional BSE image and corresponding EDS mappings of GTYL-4 h. GTYL-4 h maintains an identical corrosion structure to GTYL-1 h (Fig. 5(a)), comprising a residual

CMAS glass layer (P5), a continuous apatite reaction layer (P6), and the uncorroded substrate (P7), with minor cyclosilicate (P8) at the CMAS/apatite interface. What should be noted is that the apatite layer thickness in GTYL-4 h measures 89.8 μm, representing a significant increase from 61.9 μm observed in GTYL-1 h (Fig. 5(a)). This thickness evolution demonstrates the continuous progression of the corrosion reaction described by Eq. 1 during the 1-4 h exposure period. Fig. 5(c) presents the BSE-EDS analysis of GTYL-50 h. Similar to GTYL-1 h and GTYL-4 h, the cross-section of GTYL-50 h is also comprised with residual CMAS glass (P9), continuous apatite layer (P10) and uncorroded GTYL (P11). Notably, the apatite layer thickness in GTYL-50 h is about 96.9 μm, which is comparable to that in GTYL-4 h (89.8 μm), indicating that the nucleation of apatite grains from the CMAS melt is significantly limited during the 4-50 h corrosion period. A new reaction zone, which consists of apatite (P12), GTYL disilicate (P13) and penetrated CMAS (P14) as identified by the corresponding elemental compositions in Table 3, can be observed between the continuous apatite layer and uncorroded GTYL. Obviously, this zone is formed by the reaction between GTYL and the penetrated CMAS (P14) that has passed through the continuous apatite layer. Herein, it is defined as the "penetrated zone". What should be mentioned is that the elemental composition at point P15 (Table 3) indicates CMAS penetration into GTYL material along grain boundaries, which are recognized as weaker pathways in disilicate materials and are preferentially penetrated by CMAS during corrosion [22,30,84]. This phenomenon explained the formation mechanism of the penetrated zone: The intergranular penetration results in GTYL grains detaching from the corrosion front and entering the CMAS melt to further promote apatite precipitation and growth (P13 in Fig. 5(c)). Such unconstrained grains formed by CMAS penetration are herein defined as the "detached grains". Further analysis of EDS compositional data in Table 3 reveals that the detached GTYL grains (P13, Fig. 5(c)) in the penetration zone exhibit lower Gd content but higher Tm, Yb, and Lu concentrations than the initial $(Gd_{1/4}Tm_{1/4}Yb_{1/4}Lu_{1/4})_2Si_2O_7$ grains, revealing distinct dissolution tendencies of RE elements during CMAS corrosion. Moreover, it is worth noting that although the detached GTYL grains still react with

the penetrated CMAS, the contribution of the formed apatite to thickening the apatite layer is negligible. Compared with GTYL-1 h and GTYL-4 h, this significant difference indicates a shift in corrosion behaviors, which is attributed to the lower reactivity of penetrated CMAS compared to the initial CMAS.

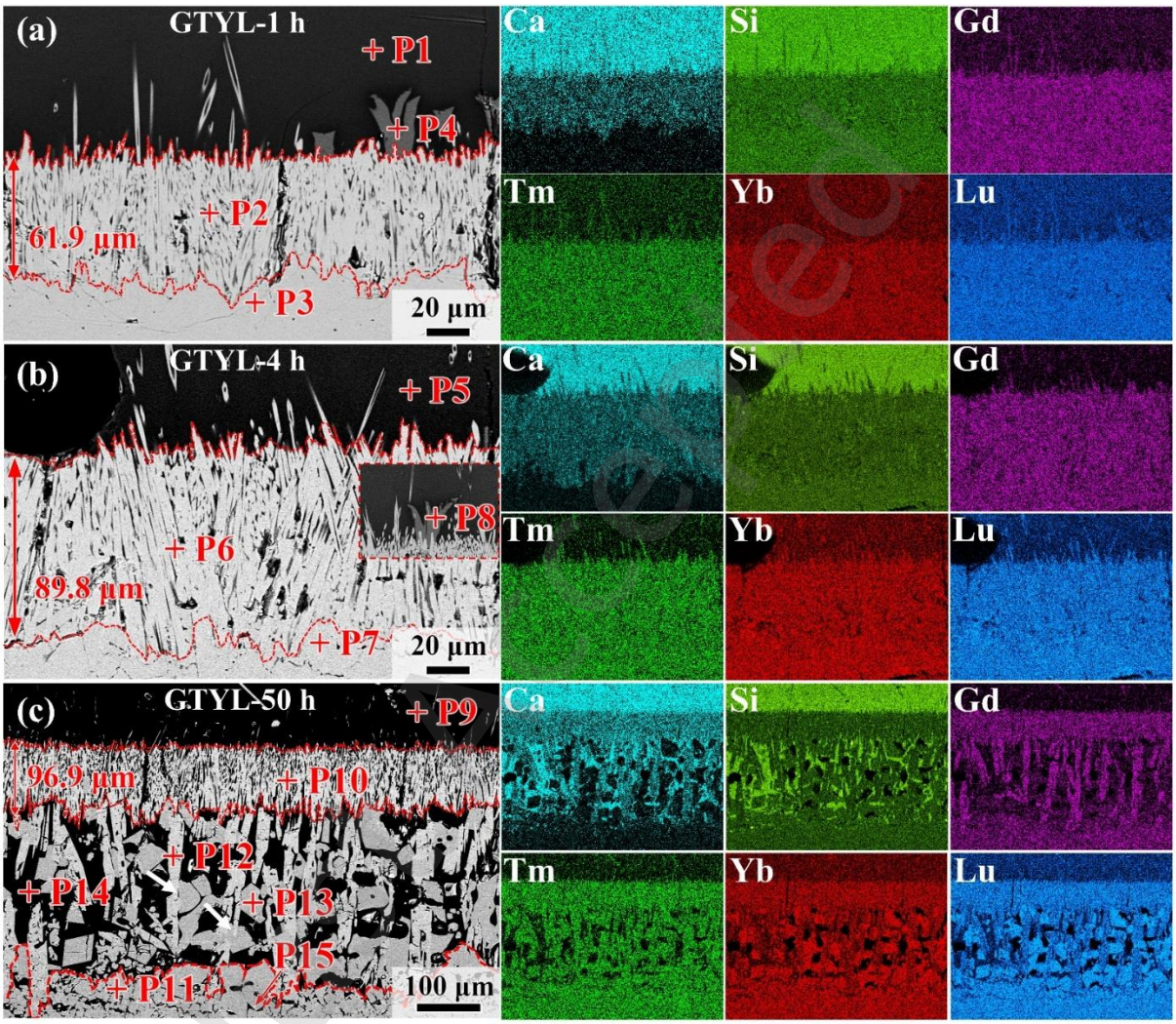

Fig. 5 Microstructures and corresponding EDS elemental mappings of $(Gd_{1/4}Tm_{1/4}Yb_{1/4}Lu_{1/4})_2Si_2O_7$ after CMAS corrosion at 1300 °C for (a) 1 h, (b) 4 h, and (c) 50 h.

Table 3 Elemental composition (in mol%, obtained from SEM-EDS data) from regions in Fig. 5 of $(Gd_{1/4}Tm_{1/4}Yb_{1/4}Lu_{1/4})_2Si_2O_7$ after CMAS corrosion at 1300 °C for 1 h, 4 h, and 50 h.

Point	CaO	MgO	$AlO_{1.5}$	SiO_2	$GdO_{1.5}$	$TmO_{1.5}$	$YbO_{1.5}$	$LuO_{1.5}$	Phase
P1	23.38 ± 0.44	4.85 ± 0.21	9.95 ± 0.60	52.29 ± 0.46	2.11 ± 0.23	2.29 ± 0.14	2.54 ± 0.23	2.60 ± 0.18	CMAS
P2	10.15 ± 0.42	/	/	45.64 ± 0.51	12.29 ± 0.19	11.05 ± 0.28	10.69 ± 0.36	10.19 ± 0.44	Apatite
P3	/	/	/	58.86 ± 0.90	9.44 ± 0.39	10.13 ± 0.36	10.74 ± 0.30	10.82 ± 0.40	Disilicate
P4	24.43 ± 0.30	/	/	55.93 ± 0.43	4.43 ± 0.23	4.87 ± 0.21	5.16 ± 0.25	5.17 ± 0.26	Cyclosilicate
P5	21.52 ± 0.34	4.13 ± 0.39	10.02 ± 0.61	53.83 ± 0.60	2.25 ± 0.14	2.53 ± 0.17	2.79 ± 0.23	2.92 ± 0.18	CMAS
P6	11.13 ± 0.28	/	/	42.61 ± 0.33	12.87 ± 0.30	11.14 ± 0.23	11.25 ± 0.33	11.00 ± 0.50	Apatite
P7	/	/	/	54.61 ± 0.65	6.17 ± 0.21	11.76 ± 0.36	13.18 ± 0.37	14.28 ± 0.21	Disilicate
P8	23.23 ± 0.26	/	/	57.05 ± 0.31	3.77 ± 0.18	5.01 ± 0.06	5.39 ± 0.24	5.55 ± 0.41	Cyclosilicate
P9	16.26 ± 0.15	6.74 ± 0.17	12.23 ± 0.35	57.93 ± 0.21	1.79 ± 0.09	1.62 ± 0.09	1.73 ± 0.11	1.69 ± 0.10	CMAS
P10	11.14 ± 0.27	/	/	44.03 ± 0.77	12.41 ± 0.35	11.12 ± 0.31	10.86 ± 0.28	10.44 ± 0.30	Apatite
P11	/	/	/	54.69 ± 0.47	5.88 ± 0.26	12.35 ± 0.27	13.41 ± 0.41	13.67 ± 0.30	Disilicate
P12	11.11 ± 0.18	/	/	43.67 ± 0.43	16.39 ± 0.11	10.49 ± 0.34	9.67 ± 0.16	8.67 ± 0.16	Apatite
P13	/	/	/	56.32 ± 0.38	5.20 ± 0.42	11.31 ± 0.23	13.01 ± 0.18	14.16 ± 0.34	Disilicate
P14	16.66 ± 0.13	6.88 ± 0.22	12.34 ± 0.46	59.60 ± 0.25	1.40 ± 0.05	1.07 ± 0.06	1.07 ± 0.08	0.97 ± 0.10	CMAS
P15	15.22 ± 0.14	6.34 ± 0.10	11.40 ± 0.40	62.36 ± 0.15	1.87 ± 0.04	1.00 ± 0.10	0.95 ± 0.04	0.86 ± 0.07	CMAS

Figure 6 displays the microstructural evolution of $(Ho_{1/4}Tm_{1/4}Yb_{1/4}Lu_{1/4})_2Si_2O_7$ during CMAS corrosion (1-50 h), with cross-sectional BSE-EDS analysis revealing phase distributions whose quantitative compositions are tabulated in Table 4. An integrated analysis of morphologies in Figs. 6(a) and 6(b) and the compositional data in Table 4 reveals three distinct zones in the cross-section of HTYL-1 h and HTYL-4 h: residual CMAS glass layer (P1 and P4), continuous apatite layers (P2 and P5) and uncorroded HTYL (P3 and P6), which is similar to that of GTYL-1 h and GTYL-4 h. Evidently, the reaction described in Eq. 1 also took place between $(Ho_{1/4}Tm_{1/4}Yb_{1/4}Lu_{1/4})_2Si_2O_7$ and CMAS, and $(Ho_{1/4}Tm_{1/4}Yb_{1/4}Lu_{1/4})_2Si_2O_7$ experienced similar corroded process with $(Gd_{1/4}Tm_{1/4}Yb_{1/4}Lu_{1/4})_2Si_2O_7$ in initial 1 to 4 hours. However, after 50 hours of corrosion, significant changes occurred on the cross-section of HTYL-50 h. As shown in Fig. 6(c), the top-layer of cross-section of $(Ho_{1/4}Tm_{1/4}Yb_{1/4}Lu_{1/4})_2Si_2O_7$ after 50 h corrosion exhibits no obvious residual CMAS layer. Instead, a continuous apatite layer (confirmed by the elemental compositions analysis at point P7 (Table 4)) covers the surface. Beneath this layer, a penetration zone containing penetrated CMAS (P8) and needle-like apatite grains (P9) is observed. The appearance of this penetration zone indicates a change in corrosion pattern during the 4-50 h period. Notably, almost no detached HTYL grains are observed in the penetration zone, indicating that HTYL material may exhibit reduced grain boundary penetration compared with GTYL. Besides, some vertical apatite grains, indicated by white arrows in Fig. 7(c), are observed to be embedded within the corrosion front. This occurs because the HTYL grains at corrosion front continuously dissolve into CMAS melt, thereby forming a source of RE release and inducing the vertical downward growth of apatite grains. This is comparable to the previous phenomenon where the apatite grains embedded in the detached GTYL grains in the penetration zone of GTYL-50 h (indicated by white arrows in Fig. 6(c)).

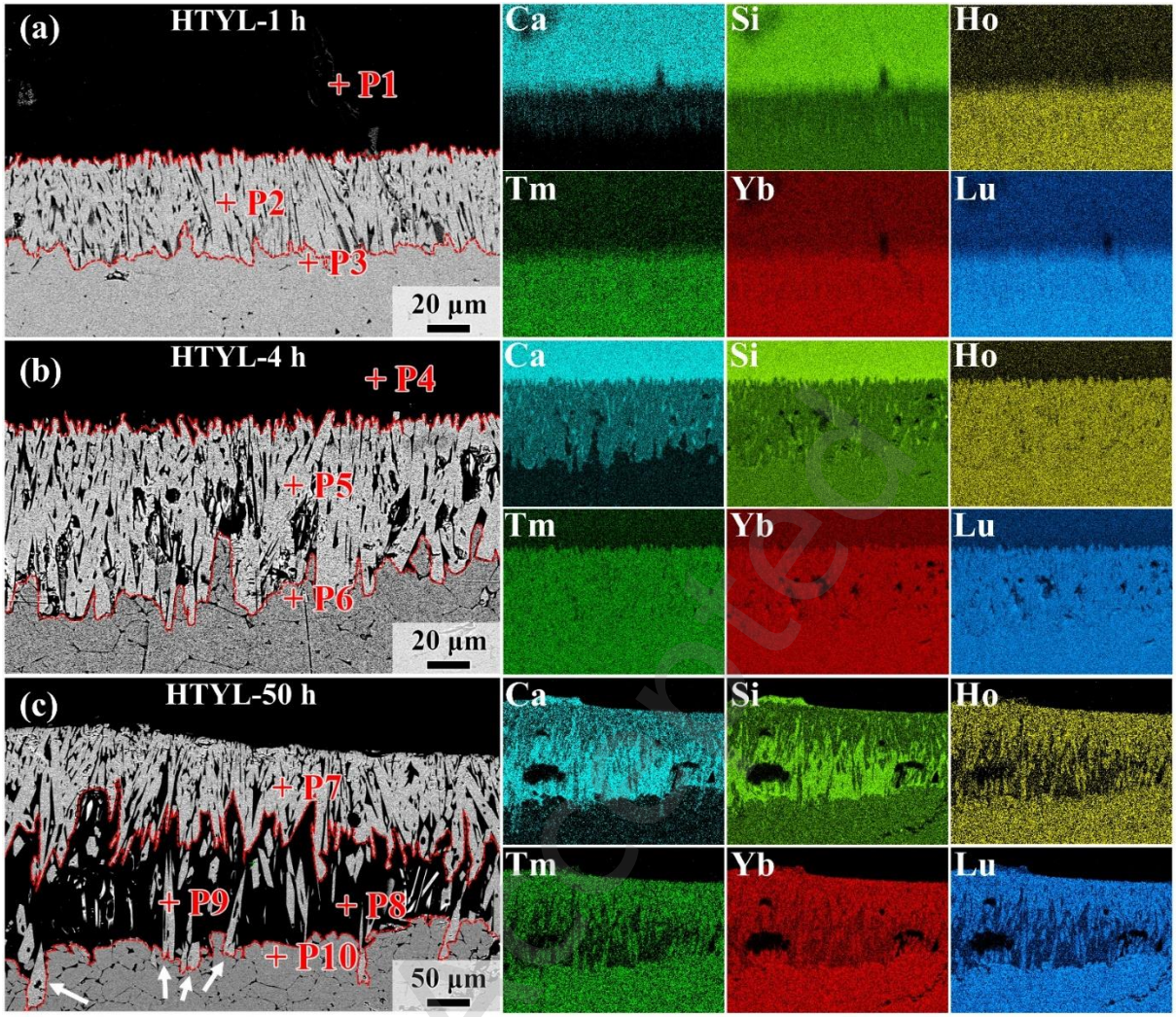

Fig. 6 Microstructures and corresponding EDS elemental mappings of $(Ho_{1/4}Tm_{1/4}Yb_{1/4}Lu_{1/4})_2Si_2O_7$ after CMAS corrosion at 1300 °C for (a) 1 h, (b) 4 h, and (c) 50 h.

Table 4 Elemental composition (in mol%, obtained from SEM-EDS data) from regions in Fig. 6 of $(Ho_{1/4}Tm_{1/4}Yb_{1/4}Lu_{1/4})_2Si_2O_7$ after CMAS corrosion at 1300 °C for 1 h, 4 h, and 50 h.

Point	CaO	MgO	$AlO_{1.5}$	SiO_2	$HoO_{1.5}$	$TmO_{1.5}$	$YbO_{1.5}$	$LuO_{1.5}$	Phase
P1	23.91 ± 0.19	7.09 ± 0.16	11.99 ± 0.47	50.50 ± 0.23	1.53 ± 0.10	1.63 ± 0.13	1.69 ± 0.15	1.66 ± 0.09	CMAS
P2	11.67 ± 0.29	/	/	43.44 ± 0.50	11.99 ± 0.33	11.32 ± 0.25	11.09 ± 0.20	10.50 ± 0.27	Apatite
P3	/	/	/	56.77 ± 0.96	10.83 ± 0.37	10.82 ± 0.25	10.89 ± 0.36	10.69 ± 0.28	Disilicate
P4	22.21 ± 0.28	6.97 ± 0.23	12.34 ± 0.69	51.14 ± 0.30	1.75 ± 0.06	1.78 ± 0.09	1.87 ± 0.15	1.94 ± 0.16	CMAS
P5	12.67 ± 0.20	/	/	43.29 ± 0.46	11.69 ± 0.16	10.96 ± 0.30	10.86 ± 0.26	10.53 ± 0.29	Apatite
P6	/	/	/	55.23 ± 0.42	11.22 ± 0.29	11.01 ± 0.25	11.25 ± 0.33	11.29 ± 0.23	Disilicate
P7	13.62 ± 1.34	/	/	38.61 ± 0.87	12.74 ± 0.71	11.97 ± 0.58	11.89 ± 0.46	11.17 ± 0.78	Apatite
P8	19.37 ± 0.28	6.65 ± 0.22	12.44 ± 0.54	56.06 ± 0.15	1.29 ± 0.05	1.34 ± 0.08	1.44 ± 0.10	1.42 ± 0.12	CMAS
P9	11.39 ± 0.30	/	/	43.59 ± 0.36	12.27 ± 0.26	11.34 ± 0.11	11.06 ± 0.23	10.35 ± 0.33	Apatite
P10	/	/	/	56.99 ± 0.36	6.95 ± 0.17	9.96 ± 0.12	12.03 ± 0.36	14.07 ± 0.20	Disilicate

Figure 7 presents the cross-sectional BSE images and representative EDS mapping results of $(Sc_{1/4}Tm_{1/4}Yb_{1/4}Lu_{1/4})_2Si_2O_7$ specimens after 1-50 hours of corrosion. The corresponding EDS elemental composition results for all identified phases are summarized in Table 5. For the 1-hour corroded sample (Fig. 7(a)), morphology and elemental data (Table 5) identify residual CMAS glass (P1), uncorroded area (P2), STYL grains with sharp-edged (P3) and with equiaxed block-shape (P4). In comparison, STYL-4 h sample (Fig. 7(b)) exhibits a greater number of equiaxed STYL grains (P7) besides the residual CMAS glass (P5) and the sharp-edged STYL grains (P6). The equiaxed block-shaped grains within the CMAS glass demonstrate morphological similarities to the $(Sc_{1/4}Tm_{1/4}Yb_{1/4}Lu_{1/4})_2Si_2O_7$ grains observed at the corrosion front (denoted by white dashed box in Fig. 7(b)), indicating that the equiaxed block-shaped grains are also formed due to CMAS penetration along the grain boundaries of STYL, namely detached STYL grains. The sharp-edged grains are deduced to be reprecipitated $(Sc_{1/4}Tm_{1/4}Yb_{1/4}Lu_{1/4})_2Si_2O_7$ grains during corrosion, and similar phenomena have been observed in previous works on CMAS corrosion of $(Er_{1/4}Tm_{1/4}Yb_{1/4}Lu_{1/4})_2Si_2O_7$ [47] and YSZ [85]. This illustrated that the CMAS corrosion pattern of STYL follows a "dissolution and re-precipitation" of $(Sc_{1/4}Tm_{1/4}Yb_{1/4}Lu_{1/4})_2Si_2O_7$ progress. Specifically, STYL continuously dissolves into CMAS and re-precipitates with the stoichiometric ratio of $RE_2Si_2O_7$ when the melt becomes supersaturated, finally form the sharp-edged STYL grains (P3 and P6 in Fig. 7) in CMAS melt. Figs. 7(c) and 7(d) show the low- and high-magnification cross-sectional BSE images of $(Sc_{1/4}Tm_{1/4}Yb_{1/4}Lu_{1/4})_2Si_2O_7$ after reaction with CMAS at 1300 °C for 50 hours, respectively. Notably, the upper section of STYL-50 h shows no detectable CMAS residue layer. As indicated by the white dashed line in Fig. 7(c), the interface between corroded and uncorroded regions is clearly delineated, and the corrosion-affected zone consists of cavities, large bulges and blister cracks. From the magnified image in Fig. 7(d), one can see that the corrosion-affected area primarily consists of brighter-contrast equiaxed grains (P8) and intergranular phases with dark contrast (P9). Based on the EDS elemental compositions data in Table 5, these two phases are recognized as detached $(Sc_{1/4}Tm_{1/4}Yb_{1/4}Lu_{1/4})_2Si_2O_7$

grain (P8) and residual CMAS (P9), respectively. This indicates that during the reaction between $(Sc_{1/4}Tm_{1/4}Yb_{1/4}Lu_{1/4})_2Si_2O_7$ and CMAS, the infiltration of CMAS along grain boundaries was more severe than in $(Gd_{1/4}Tm_{1/4}Yb_{1/4}Lu_{1/4})_2Si_2O_7$ and $(Ho_{1/4}Tm_{1/4}Yb_{1/4}Lu_{1/4})_2Si_2O_7$ materials. This severe penetration of CMAS induces stress concentrations and abnormal expansion gradients during the cooling stage [23,86]. These stress concentrations ultimately cause material delamination, manifested as cavities and surface bulges. Additionally, the abnormal expansion gradient contributes to the formation of continuous "blister cracks" within the corrosion-affected zone of $(Sc_{1/4}Tm_{1/4}Yb_{1/4}Lu_{1/4})_2Si_2O_7$.

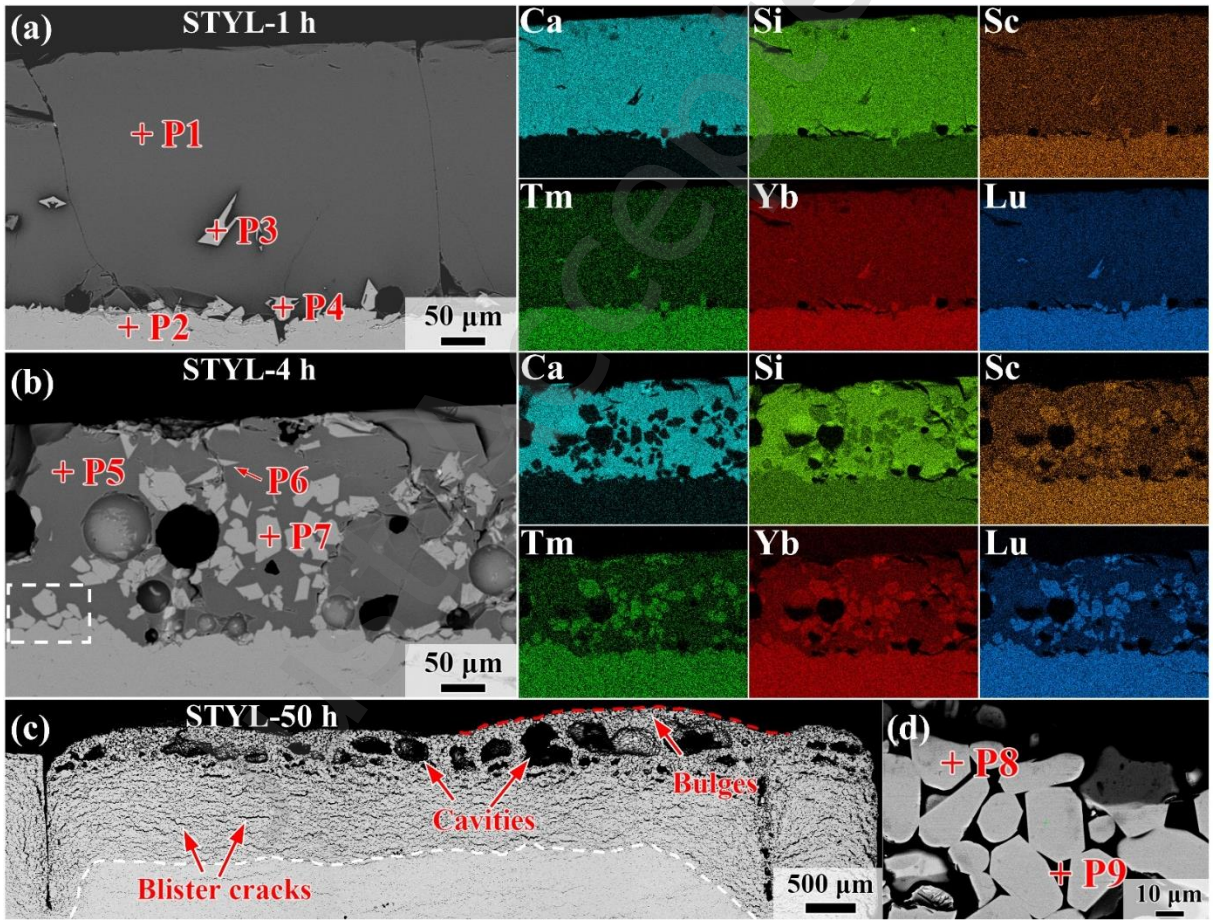

Fig. 7 Microstructures and corresponding EDS elemental mappings of $(Sc_{1/4}Tm_{1/4}Yb_{1/4}Lu_{1/4})_2Si_2O_7$ after CMAS corrosion at 1300 °C for (a) 1 h and (b) 4 h, and (c) low- and (d) high-magnification BSE images for STYL-50 h.

Table 5 Elemental composition (in mol%, obtained from SEM-EDS data) from regions in Fig. 7 of $(Sc_{1/4}Tm_{1/4}Yb_{1/4}Lu_{1/4})_2Si_2O_7$ after CMAS corrosion at 1300 °C for 1 h, 4 h, and 50 h.

Point	CaO	MgO	$AlO_{1.5}$	SiO_2	$ScO_{1.5}$	$TmO_{1.5}$	$YbO_{1.5}$	$LuO_{1.5}$	Phase
P1	23.20 ± 0.23	6.82 ± 0.18	11.34 ± 0.45	49.46 ± 0.32	2.29 ± 0.15	2.30 ± 0.09	2.37 ± 0.16	2.21 ± 0.08	CMAS
P2	/	/	/	56.79 ± 0.27	11.05 ± 0.19	10.66 ± 0.10	10.87 ± 0.27	10.63 ± 0.18	Disilicate
P3	/	/	/	56.57 ± 0.22	10.60 ± 0.27	9.88 ± 0.27	10.95 ± 0.18	11.99 ± 0.14	Disilicate
P4	/	/	/	57.30 ± 0.33	11.63 ± 0.19	9.26 ± 0.18	10.37 ± 0.21	11.43 ± 0.17	Disilicate
P5	24.98 ± 0.33	6.30 ± 0.29	11.39 ± 0.52	49.98 ± 0.43	1.85 ± 0.17	1.93 ± 0.13	1.87 ± 0.18	1.71 ± 0.05	CMAS
P6	/	/	/	55.60 ± 0.39	11.96 ± 0.21	10.44 ± 0.23	10.98 ± 0.18	11.02 ± 0.20	Disilicate
P7	/	/	/	56.26 ± 0.39	11.08 ± 0.27	10.73 ± 0.31	11.22 ± 0.19	10.71 ± 0.23	Disilicate
P8	/	/	/	50.71 ± 0.88	12.31 ± 0.23	12.23 ± 0.24	12.49 ± 0.22	12.26 ± 0.40	Disilicate
P9	26.58 ± 0.15	7.95 ± 0.13	13.77 ± 0.21	46.70 ± 0.11	1.39 ± 0.08	1.41 ± 0.10	1.18 ± 0.06	1.02 ± 0.05	CMAS

3.3 Corrosion mechanism and synergistic effect of RE elements

From the above results, we see that the ceramics investigated, $(Gd_{1/4}Tm_{1/4}Yb_{1/4}Lu_{1/4})_2Si_2O_7$, $(Ho_{1/4}Tm_{1/4}Yb_{1/4}Lu_{1/4})_2Si_2O_7$ and $(Sc_{1/4}Tm_{1/4}Yb_{1/4}Lu_{1/4})_2Si_2O_7$, exhibit significant differences in corrosion behavior when exposed to CMAS at 1300 °C. Evidently, these differences may be attributed to variations in phase structure or rare-earth components. As illustrated by Sun et al [47,48], the degradation of rare-earth disilicates through a sequential process of material dissolution and further chemical reactions in CMAS melt. According to the fact that essential difference between phase structures lies in the covalent band strength between RE-O and Si-O, this difference can only affect material dissolution but cannot control subsequent chemical reactions during CMAS corrosion progress. Therefore, componential rare-earth species remain the decisive factor in regulating corrosion progress and products [87]. It is notable that only approximately 25% of the RE elements were replaced in the $(4RE_{1/4})_2Si_2O_7$ composition. These findings warrant further investigation into the influence of RE species and their synergistic effects on the corrosion mechanisms. As noted previously, the primary degradation mechanisms of $RE_2Si_2O_7$ EBCs under CMAS attack involve either chemical reactions that progressively consume the coating material or intergranular penetration of molten CMAS along grain boundaries of $RE_2Si_2O_7$ and reaction products; both ultimately lead to coating failure. Among these mechanisms, the former is governed by two key factors: (1) the corrosion activity of CMAS, evaluated by its Ca/Si ratio as suggested by Poerschke et al. [67,88]; and (2) the chemical stability of $RE_2Si_2O_7$ and its reaction products at high-temperature CMAS exposure, which depends critically on the RE elements in their compositions [26,30]. The latter mechanism is related to the stability of $RE_2Si_2O_7$ grain boundaries or the morphology of the reaction product layer-including characteristics such as thickness, porosity and grain size. These factors collectively influence the transport of molten CMAS necessary to sustain the corrosion reactions [60,75,89]. Given that the CMAS attack on these three $RE_2Si_2O_7$ ceramics revealed both material consumption and grain boundary penetration, we further assessed the CMAS corrosion activity by measuring the distribution and content of key constituents

(Ca, Si and rare-earth elements) in the residual CMAS, $RE_2Si_2O_7$ and corrosion-formed apatite phase, alongside apatite morphological characteristics, to assess the influence of RE elements on the degradation of $RE_2Si_2O_7$.

Figure 8(a) displays the Ca/Si ratios in the residual CMAS for $(Gd_{1/4}Tm_{1/4}Yb_{1/4}Lu_{1/4})_2Si_2O_7$, $(Ho_{1/4}Tm_{1/4}Yb_{1/4}Lu_{1/4})_2Si_2O_7$, and $(Sc_{1/4}Tm_{1/4}Yb_{1/4}Lu_{1/4})_2Si_2O_7$ specimens after 1, 4 and 50 h for reaction. It is observed that the Ca/Si ratio in both GTYL and HTYL decreases continuously with prolonged exposure to the CMAS melt, whereas STYL shows the opposite trend. For specimens subjected to identical CMAS exposure times, GTYL consistently exhibits a lower Ca/Si ratio than HTYL. For instance, after 50 h CMAS corrosion, the Ca/Si ratios are approximately 0.28 for GTYL and 0.35 for HTYL, respectively. Conversely, the Ca/Si ratio in STYL specimens exhibits an anomalous increasing trend with prolonged corrosion time. This primarily stems from the different response to CMAS attack of rare-earth components in $(Sc_{1/4}Tm_{1/4}Yb_{1/4}Lu_{1/4})_2Si_2O_7$ versus $(Gd_{1/4}Tm_{1/4}Yb_{1/4}Lu_{1/4})_2Si_2O_7$ and $(Ho_{1/4}Tm_{1/4}Yb_{1/4}Lu_{1/4})_2Si_2O_7$. For STYL, dissolution of $(Sc_{1/4}Tm_{1/4}Yb_{1/4}Lu_{1/4})_2Si_2O_7$ continuously occurred during the initial corrosion stage (0-1 h, or potentially shorter), releasing RE^{3+} and Si^{4+} ions into the CMAS. This dissolution reduced the Ca/Si ratio from 0.72 (initial) to 0.47 (1 h). Subsequently, RE^{3+} and Si^{4+} in the molten CMAS re-precipitate as $(Sc_{1/4}Tm_{1/4}Yb_{1/4}Lu_{1/4})_2Si_2O_7$ grains (P3 in Fig. 7(a) and P6 in Fig. 7(b)) instead of apatite. This process decreased the Si^{4+} concentration in CMAS, increasing the Ca/Si ratio to 0.50 after 4 h and 0.57 after 50 h of corrosion. As Webster et al. [15] reported, the viscosity of CMAS melt decreases as the Ca/Si ratio increases; this reduced viscosity accelerates the melt penetration. Consequently, the incomplete penetration of CMAS into GTYL-50 h (Fig. 5(c)) benefited from its greater reduction in the Ca/Si ratio compared to HTYL-50 h (Fig. 6(c)) and STYL-50 h (Fig. 7(c)). In addition, during the corrosion of $(Sc_{1/4}Tm_{1/4}Yb_{1/4}Lu_{1/4})_2Si_2O_7$, the higher Ca/Si ratio and the resultant decrease in CMAS viscosity enhanced CMAS melt penetration into the STYL material, ultimately leading to the catastrophic failure in STYL-50 h (Fig. 7(c)).

Figure 8(b) presents a quantification of the recession depths across $(Gd_{1/4}Tm_{1/4}Yb_{1/4}Lu_{1/4})_2Si_2O_7$, $(Ho_{1/4}Tm_{1/4}Yb_{1/4}Lu_{1/4})_2Si_2O_7$, and $(Sc_{1/4}Tm_{1/4}Yb_{1/4}Lu_{1/4})_2Si_2O_7$ specimens after CMAS corrosion for different durations. The recession depth herein is defined as the average distance between the original specimen surface and the corrosion front, which was obtained from a panoramic BSE image covering the entire cross-section of the corroded specimen. Specifically, each panoramic BSE image is a composite image composed of ~15 several images at 100 × magnification and can cover the area from the surface to the corrosion front. An equidistant sampling method was employed, and the final recession depth is the average of 30 measurements. Considering the uneven corrosion depths caused by the tension and flowability of CMAS melt, we further calculated the standard error of the mean. In this study, the recession depth is serving as a quantitative indicator of the corrosion resistance ability of rare-earth disilicate. As expected, the recession depths increased with exposure duration across all specimens (Fig. 8(b)). After 50 hours, measured depths reached 256.6 μm for $(Ho_{1/4}Tm_{1/4}Yb_{1/4}Lu_{1/4})_2Si_2O_7$, 327.7 μm for $(Gd_{1/4}Tm_{1/4}Yb_{1/4}Lu_{1/4})_2Si_2O_7$, and 1014.5 μm for $(Sc_{1/4}Tm_{1/4}Yb_{1/4}Lu_{1/4})_2Si_2O_7$, respectively. Among them, GTYL and HTYL consistently exhibit similar recession depth trends. For comparison, STYL exhibited a comparable recession depth trend to GTYL and HTYL during the initial reaction phase (1-4 h). Beyond 4 hours, however, STYL displayed a distinct acceleration in recession depth increase, ultimately reaching a maximum depth of 1014.5 μm at 50 hours.

Obviously, a difference exists in the kinetic process of CMAS corrosion between STYL and the other two $(xRE_{1/x})_2Si_2O_7$. To further quantitatively compare these kinetic differences, we also calculated the recession rate by using the ratio of recession depth to corrosion time and plotted its correlation curves against the corrosion times (Fig. 8(c)). As seen, both GTYL and HTYL exhibit gradually decaying trends, which indicates that the recession has been gradually alleviated during the corrosion process. However, the recession rate of STYL shows a decreasing trend, dropping from 53.6 μm/h to 20.1 μm/h within only the initial 4 hours, and then remains at a high constant level of

approximately 20 μm/h. Thus, although STYL exhibits minimal corrosion during the initial 0-4 h period due to its strong intrinsic resistance to CMAS corrosion (Fig. 8b)) compared with GTYL and HTYL, the subsequently progressive penetration of CMAS at a rate of around 20 μm/h ultimately results in the maximum recession depth in STYL after 50 h (Fig. 8(b)). To sum up, STYL mainly manifests the resistance in the dissolution stage within the initial 4 hours, and has almost no ability to alleviate the recession in the subsequent corrosion process. By comparison, GTYL and HTYL can be classified into a same category due to their recession similarity. However, it is notable that GTYL consistently demonstrated a greater recession depth and a higher recession rate than HTYL throughout the entire corrosion period. This observation seems inconsistent with the previous findings in Fig. 9(a) that a lower Ca/Si ratio in GTYL's residual CMAS may help reduce the CMAS corrosion activity and enhance the material's resistance. To address this, we further characterized the morphological properties of the apatite layer formed as a reaction product, aiming to provide an explanation from the perspective of CMAS transport.

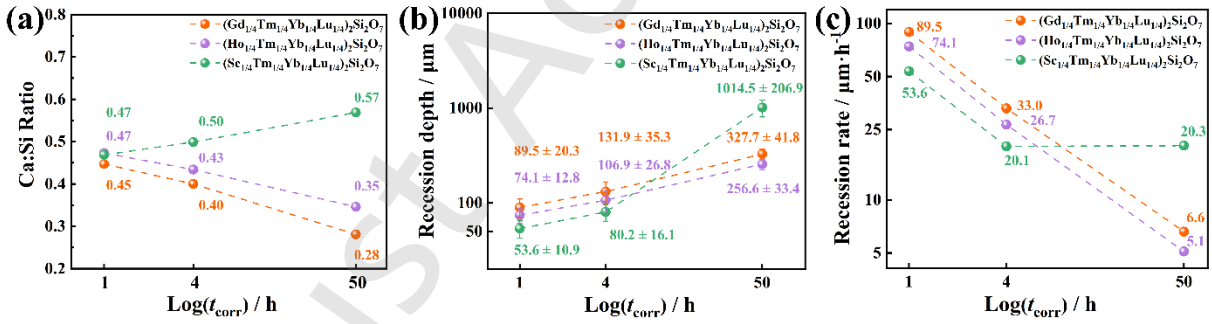

Fig. 8 Residual Ca/Si ratio (a), average recession depth (b), and the recession rate (c) of three multicomponent rare-earth disilicates after CMAS corrosion at 1300 °C.

Three quantitative statistical indicators, namely the thickness of apatite layer, the grain aspect ratio (length to diameter ratio, L/D) of apatite, and the porosity within apatite layers, were measured from the corroded cross sections of GTYL and HTYL and plotted in Figs. 9(a)-9(c) to elucidate the specific contributions of the rare-earth elements Gd and Ho to CMAS corrosion kinetics. Similar to the measurements of corrosion depth, the acquirements of apatite layer thickness are also based on the corresponding panoramic BSE images and use the same equidistant sampling method with 30

measurements per specimen. Furthermore, five 500 × magnification BSE images were collected as a more refined statistical dataset to calculate the L/D ratio and the porosity. Specifically, the final L/D ratio is the mean L/D of 50 different apatite grains randomly selected in the apatite layers from these BSE images. Meanwhile, the porosity in whole apatite layer represents the average value of the local porosity (the ratio of pore area to the whole area of the view field) obtained from each BSE image. As illustrated in Fig. 9(a), the thickness of the apatite layers in GTYL and HTYL increased significantly within the initial 4 hours, followed by a decreased growth in 4-50 h period. It is notable that the apatite layer in GTYL consistently exhibits a greater thickness, indicating a more active reactivity to CMAS compared with HTYL. Thus, the greater recession depth (Fig. 8(b)) and the higher recession rate (Fig. 8(c)) of GTYL are clearly attributed to the accelerated reaction (Eq. 1) dominated by Gd, rather than other factors such as CAMS penetration. Fig. 9(b) presents the average grain aspect ratio (L/D) of grains within the continuous apatite layers of GTYL and HTYL specimens. Both specimens exhibit a decreasing L/D ratio with prolonged corrosion time. Nevertheless, GTYL consistently maintains higher L/D values than HTYL. This elevated L/D ratio suggests that the nucleation and growth of apatite occurred more rapidly in GTYL compared to HTYL during the reaction, resulting in a greater tendency for apatite grains to develop elongated, needle-like morphologies. Evidently, this accelerated apatite formation in GTYL is the specific corresponding process of the high recession rate shown in Fig. 8(c), compared to HTYL. In addition, the elevated L/D ratio is an intuitive manifestation of the high recession rate in the corrosion product microstructures from the perspective of corrosion kinetics. Moreover, the average porosity of the continuous apatite layers in both GTYL and HTYL specimens was measured and plotted in Fig. 9(c). The porosity progressively increases with corrosion time, with HTYL consistently showing higher values than GTYL. This trend indicates a less dense apatite layer formed in HTYL compared to GTYL. The porosity characteristics of the apatite layers in GTYL and HTYL exhibit a strong correlation with the thickness and L/D ratio in the prior measurements. Specifically, higher nucleation density and grain growth rate of apatite in GTYL results in reduced

grain growth space, yielding fine and elongated apatite grains and a higher-density layer. Moreover, prior studies have demonstrated that denser apatite layers exhibit a more effective barrier against CMAS infiltration [46,60,61,64]. This is corroborated by the substantial retention of residual CMAS glass on GTYL-50 h (Fig. 5(c)), in contrast to the near-complete absence of CMAS on HTYL-50 h (Fig. 5(c)).

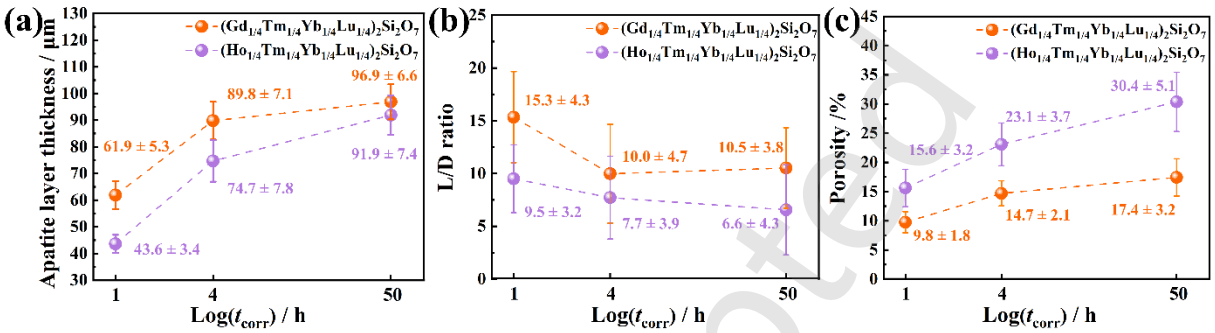

Fig. 9 Average thickness of apatite layers (a), aspect ratio of apatite grains (b), and porosity in apatite layers of three kinds of multicomponent rare-earth disilicate specimens.

As mentioned earlier, the differences in CMAS corrosion resistance behavior among $(Gd_{1/4}Tm_{1/4}Yb_{1/4}Lu_{1/4})_2Si_2O_7$, $(Ho_{1/4}Tm_{1/4}Yb_{1/4}Lu_{1/4})_2Si_2O_7$, and $(Sc_{1/4}Tm_{1/4}Yb_{1/4}Lu_{1/4})_2Si_2O_7$ materials primarily originate from the variations in their rare-earth elements. To this end, we quantified the distribution of rare-earth elements in the reactants and products for each material after different reaction times and plotted the results in Fig. 10. As shown in Fig. 10, these three materials exhibit three distinct patterns of rare-earth element distribution. Among them, GTYL and HTYL are largely comparable; the primary difference lies in the initial reaction stage (1-4 h): besides the apatite phase formed in both, rare-earth cyclosilicate was also detected in GTYL. In contrast, no apatite phase was observed in STYL. For both GTYL and HTYL, regardless of the reaction products formed, the rare-earth elements exhibit similar distribution trends. In the residual CMAS, rare-earth disilicate, and cyclosilicate phases, the contents of Gd/Ho, Tm, Yb, and Lu increase as the ionic radius of the rare-earth elements decreases. In contrast, within the apatite phase, an opposite trend is observed: their contents increase with increasing ionic radius. These findings align with the phenomenon we

previously observed in the CMAS corrosion reactions of $(Er_{1/4}Tm_{1/4}Yb_{1/4}Lu_{1/4})_2Si_2O_7$, where enhanced CMAS resistance is achieved through synergistic effects of multi principal rare-earth cations. Specifically, active elements such as Er and Tm promote rapid precipitation of apatite, accelerating the reduction in Ca/Si ratio and thereby diminishing CMAS corrosivity, while inert elements like Lu and Yb play a key role in maintaining the phase stability of disilicate during corrosion [47]. As observed in this work, the synergistic enhancement mechanism of multiple rare-earth cations remains effective even after incorporating Ho or Gd-elements with larger ionic radii-into the rare-earth disilicate system. Furthermore, as the ionic radius of active rare-earth cations in the silicate material increases, for instance, through substitution from Ho to Gd in $(4RE_{1/4})_2Si_2O_7$, their distribution across the reaction phases involved follows a distinct pattern. Overall, under identical reaction conditions, larger rare-earth cations exhibit a higher proportion in the apatite phase and a lower proportion in the rare-earth silicate phases. For example, after 4 hours of reaction, Gd accounts for 12.87 mol% in apatite (P6, Table 3) versus 6.17 mol% in the rare-earth silicate phases (P7, Table 3); conversely, Ho constitutes 11.69 mol% in apatite phase (P5, Table 4) and 11.22 mol% in the rare-earth silicate phases (P6, Table 4). This distribution difference originates from the formation enthalpy diversity of apatite containing different RE cations. Specifically, apatite with a larger average radius of RE^{3+} cations (e.g. Gd^{3+}) exhibits lower formation enthalpy under identical conditions [90]. This constitutes the mechanistic origin enabling synergistic optimization of multi principal rare-earth cations, whereby distinct RE elements differentially govern the dissolution of $(4RE_{1/4})_2Si_2O_7$ and reprecipitation of apatite during CMAS reactions with rare-earth disilicates. Furthermore, during the CMAS corrosion of STYL, $(Sc_{1/4}Tm_{1/4}Yb_{1/4}Lu_{1/4})_2Si_2O_7$ similarly dissolves into the melt during the initial reaction stage, evidenced by the comparable distribution of Sc, Tm, Yb and Lu elements in residual CMAS (Figs. 10(g)-10(i)). However, due to the absence of active elements such as Gd and Ho, apatite phase precipitation fails to occur, resulting in persistently high CMAS corrosivity, intergranular destabilization of the material and severe penetrative corrosion along grain boundaries.

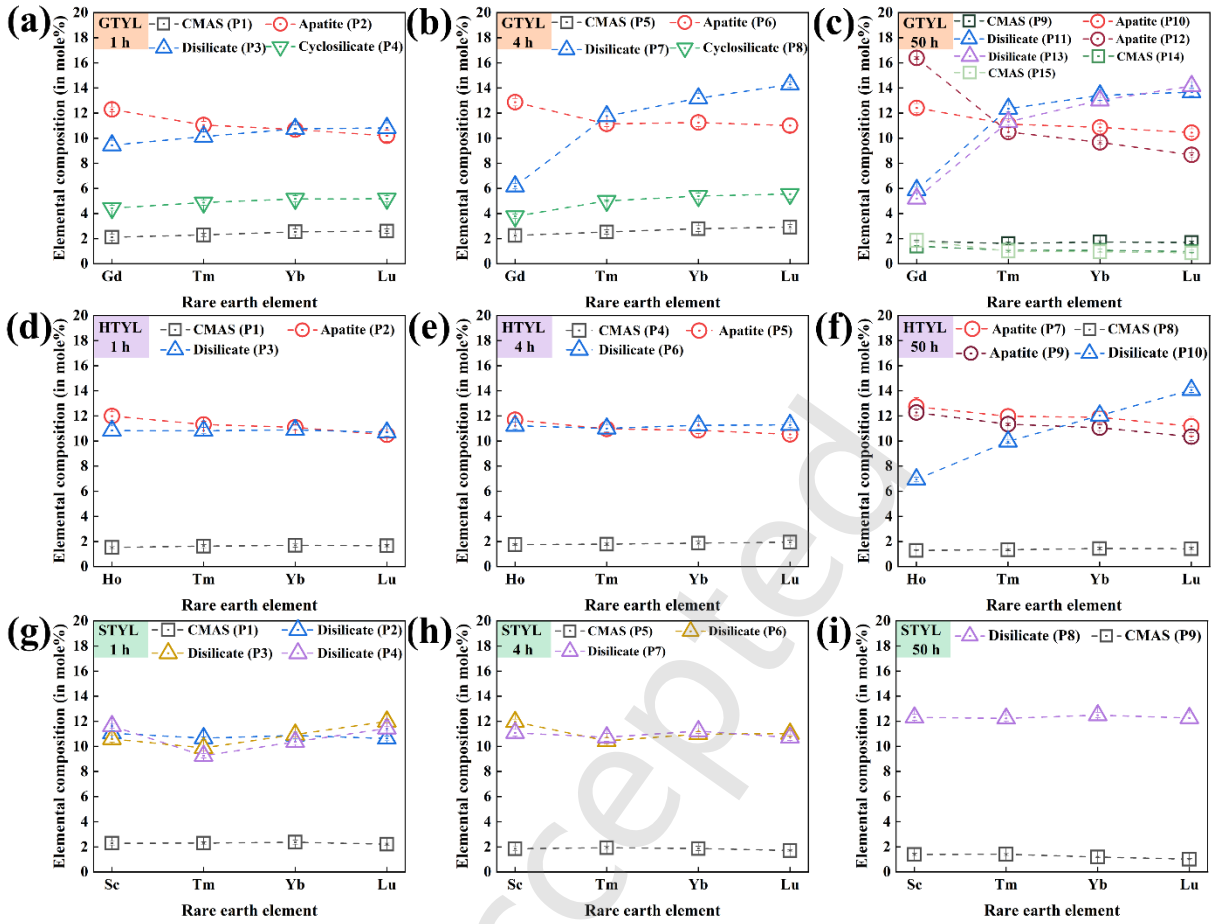

Fig. 10 Distribution of rare-earth elements in the reactants (CMAS and $(4RE_{1/4})_2Si_2O_7$) and products (apatite, cyclosilicate and re-precipitated disilicate grains) for $(Gd_{1/4}Tm_{1/4}Yb_{1/4}Lu_{1/4})_2Si_2O_7$, $(Ho_{1/4}Tm_{1/4}Yb_{1/4}Lu_{1/4})_2Si_2O_7$ and $(Sc_{1/4}Tm_{1/4}Yb_{1/4}Lu_{1/4})_2Si_2O_7$ after different reaction times with CMAS at 1300 °C.

Based on the above investigations, Fig. 11 schematically illustrates the CMAS corrosion mechanism at 1300 °C for $(4RE_{1/4})_2Si_2O_7$ systems exhibiting differential synergistic effects, as determined from the corrosion behaviors of $(Gd_{1/4}Tm_{1/4}Yb_{1/4}Lu_{1/4})_2Si_2O_7$, $(Ho_{1/4}Tm_{1/4}Yb_{1/4}Lu_{1/4})_2Si_2O_7$, and $(Sc_{1/4}Tm_{1/4}Yb_{1/4}Lu_{1/4})_2Si_2O_7$ in this study. In materials such as $(Gd_{1/4}Tm_{1/4}Yb_{1/4}Lu_{1/4})_2Si_2O_7$ and $(Ho_{1/4}Tm_{1/4}Yb_{1/4}Lu_{1/4})_2Si_2O_7$, the presence of active elements like Gd/Ho accelerates precipitation of precipitated phase, rapidly reducing the Ca/Si ratio in CMAS melt, thereby diminishing the CMAS corrosivity. This process concurrently forms a dense protective layer of vertically aligned apatite grains that impedes CMAS penetration. Concurrently, inert elements (Lu and Yb) in their composition preserve disilicate phase integrity during corrosion. Taking HTYL as an example, initial CMAS corrosion (Fig. 11(d)) involves dissolution of the disilicate into the melt. This

elevates RE^{3+} and Si^{4+} concentrations while reducing the Ca/Si ratio in the CMAS liquid, driving apatite grain precipitation at the reaction interface. As the corrosion reaction progresses, a nearly dense protective layer composed of vertical apatite grains forms, thereby delaying the penetration of CMAS (Fig. 11(e)). Also, a limited amount of cyclosilicate grains may be formed during this stage. In the subsequent stage (Fig. 11(f)), CMAS continuously penetrates through the apatite layer into the underlying disilicate with a diminished rate. Compared with the initial CMAS (0.72), the lower Ca/Si ratio (0.28, P14 in Table3) of the penetrated CMAS decrease the driving force for apatite precipitation. As a result, the apatite grains generated by the reaction are limited and dispersed, thus being unable to provide effective thickening effects for the continuous apatite layers. This relatively slow corrosion continues until the Ca/Si ratio decreases to a threshold, indicating that the whole system reaches thermodynamic equilibrium. GTYL exhibits corrosion behavior similar to HTYL during initial (Fig. 11(a)) and intermediate (Fig. 11(b)) stages, where Gd^{3+} promotes apatite layer formation and reduces the Ca/Si ratio, thereby impeding CMAS penetration. The distinction lies in the presence of Gd^{3+}, which accelerates the apatite precipitation and growth, causing excessive consumption of Ca^{2+} and RE^{3+} within the molten CMAS. Consequently, compared with HTYL, apatite precipitation becomes more difficult, and the thickness variation of the continuous apatite layers remains at a lower level in the late stage of GTYL. Meanwhile, the limited precipitation of apatite also reduces the dissolution rate of GTYL, leading to the extensive coexistence of penetrated CMAS and detached GTYL grains in the penetrated zone. To sum up, the fundamental differences between GTYL and HTYL stem from the corrosion intensity in the initial and intermediate stage, which are due to the more active reactivity of Gd. This consequently accelerates GTYL dissolution, degrades the disilicate matrix, and ultimately increases the recession depth. In contrast to GTYL and HTYL, STYL exhibits negligible synergistic effects among multiple rare-earth elements during CMAS corrosion. As illustrated in Figs. 11 (g) - 11(i), due to insufficient concentrations of active elements like Gd or Ho within the material composition to facilitate precipitation reaction products like apatite, it only temporarily increases the

RE^{3+} and Si^{4+} concentrations in the CMAS liquid and reduce the Ca/Si ratio through STYL dissolution, maintaining a relatively minimal recession depth for a short period. Once RE^{3+} reaches the critical concentration in the melt, $(Sc_{1/4}Tm_{1/4}Yb_{1/4}Lu_{1/4})_2Si_2O_7$ begins to precipitate from the liquid, leading to a continuous and slow increase in the Ca/Si ratio with the consumption of Si^{4+}. An increasing Ca/Si ratio results in decreased CMAS viscosity and enhanced penetration along grain boundaries. Consequently, numerous STYL disilicate grains are detached from the substrate during the intermediate corrosion stage (Fig. 11(h)). This mechanism persists into the late stage of corrosion, during which CMAS fully penetrates the specimen (Fig. 9(i)), accompanied by stress concentrations and localized abnormal thermal expansion gradients. These factors collectively contribute to the formation of cavities, extensive bulging, and blister cracks, indicating the complete material failure.

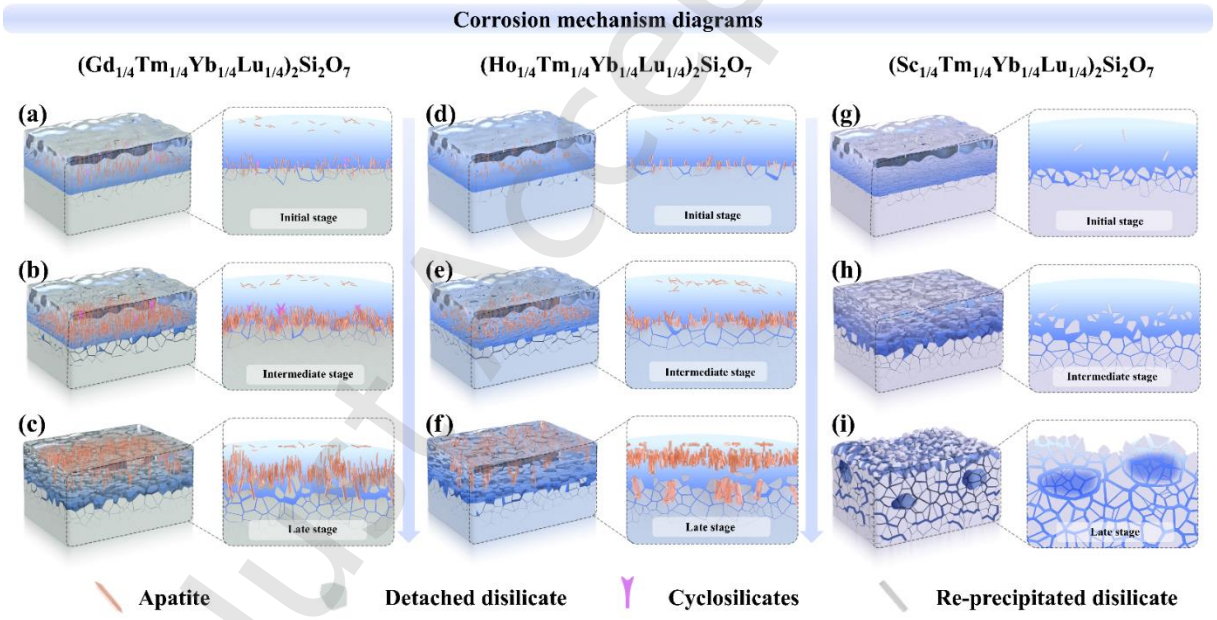

Fig. 11 Schematic diagram for the corrosion behaviors of (a-c) $(Gd_{1/4}Tm_{1/4}Yb_{1/4}Lu_{1/4})_2Si_2O_7$, (d-f) $(Ho_{1/4}Tm_{1/4}Yb_{1/4}Lu_{1/4})_2Si_2O_7$, and (g-i) $(Sc_{1/4}Tm_{1/4}Yb_{1/4}Lu_{1/4})_2Si_2O_7$ with CMAS at 1300 °C.

Based on the above analysis, it is evident that the appropriate selection of RE elements in $(4RE_{1/4})_2Si_2O_7$ is crucial for inducing synergy against CMAS attack. Specifically, during composition optimization, active components are required to consume corrosive substances and establish protective corrosion product barriers. Meanwhile, inert components should also be properly introduced to balance the overall chemical reactivity of the solid solution, thereby avoiding excessive material loss.

Nevertheless, how to precisely control the types and ratios of active and inert elements remains an unresolved critical challenge. Based on the established correlation that the enthalpy of formation for apatite progressively decreases with increasing RE^{3+} ionic radius, and considering the distinct reactivity demonstrated by $(Gd_{1/4}Tm_{1/4}Yb_{1/4}Lu_{1/4})_2Si_2O_7$, $(Ho_{1/4}Tm_{1/4}Yb_{1/4}Lu_{1/4})_2Si_2O_7$, and $(Sc_{1/4}Tm_{1/4}Yb_{1/4}Lu_{1/4})_2Si_2O_7$ systems, the optimal ionic radius range for active rare-earth components lies between Tm^{3+} and Gd^{3+} (with ion radius ranging 0.880 - 0.938 Å). Moreover, selecting inert rare-earth elements must account for their compatibility with active components, including the ability to form stable single-phase rare-earth silicates, and the capacity to maximize the synergistic effect on CMAS corrosion resistance. In this process, identifying and establishing quantitative design guidelines will enable the precise and efficient design of highly CMAS corrosion-resistant rare-earth silicate materials. For example, the optical basicity (OB) theory proposed by Duffy et al. [91] provides a feasible quantitative criterion to assign the relationship between the cations and physics and chemistry of glass. The OB theory is based on the Lewis acid-base theory. Besides the effects on the electron cloud caused by cations, the influences caused by structural factors (e.g., the "bridge atom O" in the polyhedron) are also considered. Thus, it can serve as an effective tool to estimate the chemical reactivity of rare-earth disilicates with CMAS melt and facilitate the selection of rare-earth elements [91,92]. For instance, the OB values of $\Delta\Lambda_{(GTYL\text{-}CMAS)}$, $\Delta\Lambda_{(HTYL\text{-}CMAS)}$ and $\Delta\Lambda_{(STYL\text{-}CMAS)}$ in this work are calculated as 0.037, 0.034, and 0.028, respectively. The resulting OB range of $0.028 < \Delta\Lambda_{(REDS\text{-}CMAS)} < 0.037$ could act as a rough criterion for designing multicomponent rare-earth silicates with enhanced CMAS corrosion resistance. Additionally, given the limited types of rare-earth elements available, the design space for combining inert and reactive silicate cations is constrained. Adopting equimolar or non-equimolar high-entropy or multi-component designs will significantly expand this design space. Nevertheless, substantial work remains necessary to achieve enhanced CMAS corrosion resistance in rare-earth disilicates, requiring the rational selection and proportioning of rare-earth elements to maximize their synergistic effects.

4 Conclusions

In this study, three multicomponent $(RE_{1/4}Tm_{1/4}Yb_{1/4}Lu_{1/4})_2Si_2O_7$ (RE = Gd, Ho and Sc) materials were designed and exposed to CMAS at 1300 °C for durations of 1, 4, and 50 h. The phase evolution and morphological changes were systematically characterized before and after corrosion. A detailed analysis of the role of rare-earth cations in CMAS attack was conducted by examining their influence on the formation of corrosion products. Results demonstrate that $(Gd_{1/4}Tm_{1/4}Yb_{1/4}Lu_{1/4})_2Si_2O_7$ and $(Ho_{1/4}Tm_{1/4}Yb_{1/4}Lu_{1/4})_2Si_2O_7$ possess enhanced CMAS corrosion resistance compared to $(Sc_{1/4}Tm_{1/4}Yb_{1/4}Lu_{1/4})_2Si_2O_7$, with measured recession depths reached 256.6 μm for $(Ho_{1/4}Tm_{1/4}Yb_{1/4}Lu_{1/4})_2Si_2O_7$, 327.7 μm for $(Gd_{1/4}Tm_{1/4}Yb_{1/4}Lu_{1/4})_2Si_2O_7$, and 1014.5 μm for $(Sc_{1/4}Tm_{1/4}Yb_{1/4}Lu_{1/4})_2Si_2O_7$ after 50 hours, respectively. Mechanistic analysis reveals that this performance divergence primarily stems from distinct corrosion mechanisms: $(Gd_{1/4}Tm_{1/4}Yb_{1/4}Lu_{1/4})_2Si_2O_7$ and $(Ho_{1/4}Tm_{1/4}Yb_{1/4}Lu_{1/4})_2Si_2O_7$ predominantly undergo dissolution-reprecipitation processes, whereas $(Sc_{1/4}Tm_{1/4}Yb_{1/4}Lu_{1/4})_2Si_2O_7$ is dominated by intergranular corrosion penetration. Such mechanistic transition is attributable to compositional tuning of rare-earth elements (Gd and Ho to Sc) in the silicates. Elements such as Gd and Ho reduce the Ca/Si ratios to approximately 0.28 ($(Gd_{1/4}Tm_{1/4}Yb_{1/4}Lu_{1/4})_2Si_2O_7$) and 0.35 ($(Ho_{1/4}Tm_{1/4}Yb_{1/4}Lu_{1/4})_2Si_2O_7$) by accelerating the precipitation of apatite phase during reaction. This process not only diminishes calcium in CMAS to reduce its corrosion aggressiveness but also retards CMAS diffusion through the formation of a dense product layer, collectively enhancing the corrosion resistance of disilicates. Furthermore, comparative analysis of ($(Gd_{1/4}Tm_{1/4}Yb_{1/4}Lu_{1/4})_2Si_2O_7$) and ($(Ho_{1/4}Tm_{1/4}Yb_{1/4}Lu_{1/4})_2Si_2O_7$) reveals that an optimal stoichiometric ratio between active (e.g., Gd and Ho) and inert (e.g., Yb and Lu) elements is essential to synergistically activate the precipitation for corrosion mitigation and the intrinsic resistance enhancement, thereby maximizing CMAS corrosion resistance in disilicate systems. These findings provide valuable insights for in-depth

understanding of the synergistic effects among rare-earth components and the correlation mechanism of multicomponent rare-earth disilicates.

Acknowledgements

The financial support of the National Natural Science Foundation of China (U21A2063), LiaoNing Revitalization Talents Program (XLYC2203090), and International Partnership Program of the Chinese Academy of Sciences (172GJHZ2022094FN) is gratefully acknowledged.

Funding

National Natural Science Foundation of China (U21A2063); LiaoNing Revitalization Talents Program (XLYC2203090); International Partnership Program of the Chinese Academy of Sciences (172GJHZ2022094FN).

Author contributions

Ziyu Wang: Conceptualization, methodology, data acquisition, investigation, writing-original draft & editing. **Luchao Sun:** Conceptualization, methodology, funding acquisition, writing-review & editing. **Tiefeng Du:** Investigation. **Sikai Wang:** Investigation. **Cui Zhou:** Investigation. **Yixiu Luo:** Conceptualization, methodology. **Jiemin Wang:** Conceptualization, methodology. **Jingyang Wang:** Conceptualization, funding acquisition, methodology, project administration, writing-review & editing.

Availability of data and materials

The data that support the findings of this study are available from the corresponding author upon reasonable request.

Competing interests

The authors have no competing interests to declare that are relevant to the content of this article. The author Jingyang Wang is the Editorial Committee member of this journal.

Electronic Supplementary Material

Supplementary material has been uploaded to the journal website.

References

[1] Padture NP. Advanced structural ceramics in aerospace propulsion. *Nature Mater* 2016, **15**: 804–9.
[2] Marshall DB, Cox BN. Integral textile ceramic structures. *Annu Rev Mater Res* 2008, **38**: 425–43.
[3] Presby MJ, Mansour R, Manigandan K, *et al.* Characterization and simulation of foreign object damage in curved and flat SiC/SiC ceramic matrix composites. *Ceram Int* 2019, **45**: 2635–43.
[4] Wu S, Cheng L, Zhang L, *et al.* Corrosion of SiC/SiC composite in Na_2SO_4 vapor environments from 1000 to 1500°C. *Compos Part A-appl S* 2006, **37**: 1396–401.
[5] Zhang J, Liu R, Jian Y, *et al.* Degradation mechanism of SiC_f/SiC composites after long-time water vapor and oxygen corrosion at 1300 °C. *Corros Sci* 2022, **197**: 110099.
[6] Guo F, Chen X, Yang J, *et al.* Stress-corrosion behavior of SiC_f/SiC under CMAS-wet-oxygen environments. *Corros Sci* 2024, **228**: 111844.
[7] Eaton HE, Linsey GD. Accelerated oxidation of SiC CMC's by water vapor and protection via environmental barrier coating approach. *J Eur Ceram Soc* 2002, **22**: 2741–7.
[8] Tejero-Martin D, Bennett C, Hussain T. A review on environmental barrier coatings: History, current state of the art and future developments. *J Eur Ceram Soc* 2021, **41**: 1747–68.
[9] Turcer LR, Padture NP. Towards multifunctional thermal environmental barrier coatings (TEBCs) based on rare-earth pyrosilicate solid-solution ceramics. *Scripta Mater* 2018, **154**: 111–7.
[10] Fernandez-Carrion AJ, Allix M, Becerro AI. Thermal expansion of rare-Earth pyrosilicates. *J Am Ceram Soc* 2013, **96**: 2298–305.
[11] Luo Y, Sun L, Wang J, *et al.* Material-genome perspective towards tunable thermal expansion of rare-earth di-silicates. *J Eur Ceram Soc* 2018, **38**: 3547–54.
[12] Zhu D. Advanced environmental barrier coatings for SiC/SiC ceramic matrix composite turbine components. In: *Engineered Ceramics.* Ohji T, Singh M, Eds. Wiley; 2016: 187–202.
[13] Zhao H, Richards BT, Levi CG, *et al.* Molten silicate reactions with plasma sprayed ytterbium silicate coatings. *Surf Coat Tech* 2016, **288**: 151–62.
[14] Poerschke DL, Jackson RW, Levi CG. Silicate deposit degradation of engineered coatings in gas turbines: Progress toward models and materials solutions. In: Annu Rev Mater Res. Clarke DR, Eds. Palo Alto. Annual Reviews; 2017: 297–330.
[15] Webster RI, Opila EJ. Viscosity of CaO-MgO-Al_2O_3-SiO_2 (CMAS) melts: Experimental measurements and comparison to model calculations. *J Non-Cryst Solids* 2022, **584**: 121508.
[16] Borom MP, Johnson CA, Peluso LA. Role of environmental deposits and operating surface temperature in spallation of air plasma sprayed thermal barrier coatings. *Surf Coat Technol* 1996, **86**: 116–26.
[17] Naraparaju R, Gomez Chavez JJ, Schulz U, *et al.* Interaction and infiltration behavior of Eyjafjallajökull, Sakurajima volcanic ashes and a synthetic CMAS containing FeO with/in EB-PVD ZrO_2 -65 wt% Y_2O_3 coating at high temperature. *Acta Mater* 2017, **136**: 164–80.
[18] Liu D, Song W, He W, *et al.* Modeling the viscosity and infiltration kinetics of silicate melt -thermal barrier coating systems based on deep-learning and experimental approach. *Acta Mater* 2025, **292**: 121081.
[19] Song W, Lavallée Y, Hess KU, *et al.* Volcanic ash melting under conditions relevant to ash turbine interactions. *Nat Commun* 2016, **7**: 10795.
[20] Stolzenburg F, Kenesei P, Almer J, *et al.* The influence of calcium–magnesium–aluminosilicate deposits on internal stresses in $Yb_2Si_2O_7$ multilayer environmental barrier coatings. *Acta Mater* 2016, **105**: 189–98.
[21] Poerschke DL, Hass DD, Eustis S, *et al.* Stability and CMAS resistance of ytterbium-silicate/hafnate EBCs/TBC for SiC composites. *J Am Ceram Soc* 2015, **98**: 278–86.
[22] Turcer LR, Krause AR, Garces HF, *et al.* Environmental-barrier coating ceramics for resistance against attack by molten calcia-magnesia-aluminosilicate (CMAS) glass: Part I, $YAlO_3$ and γ-$Y_2Si_2O_7$. *J Eur Ceram Soc* 2018, **38**: 3905–13.
[23] Turcer LR, Krause AR, Garces HF, *et al.* Environmental-barrier coating ceramics for resistance against attack by molten calcia-magnesia-aluminosilicate (CMAS) glass: Part II, β-$Yb_2Si_2O_7$ and β-$Sc_2Si_2O_7$. *J Eur Ceram Soc* 2018, **38**: 3914–24.
[24] Ahlborg NL, Zhu D. Calcium–magnesium aluminosilicate (CMAS) reactions and degradation mechanisms of advanced environmental barrier coatings. *Surf and Coat Tech* 2013, **237**: 79–87.
[25] Stolzenburg F, Johnson MT, Lee KN, *et al.* The interaction of calcium–magnesium–aluminosilicate with ytterbium silicate environmental barrier materials. *Surf Coat Tech* 2015, **284**: 44–50.

[26] Liu J, Zhang L, Liu Q, *et al.* Calcium-magnesium-aluminosilicate corrosion behaviors of rare-earth disilicates at 1400 °C. *J Eur Ceram Soc* 2013, **33**: 3419–28.
[27] Stokes JL, Harder BJ, Wiesner VL, *et al.* Effects of crystal structure and cation size on molten silicate reactivity with environmental barrier coating materials. *J Am Ceram Soc* 2020, **103**: 622–34.
[28] Kim SH, Nagashima N, Matsushita Y, *et al.* Interaction of $Gd_2Si_2O_7$ with CMAS melts for environmental barrier coatings. *J Eur Ceram Soc* 2023, **43**: 593–9.
[29] Chen Z, Huang Y, Zhang Z, *et al.* Investigation of improving the thermophysical properties and corrosion resistance of RE_2SiO_5/$RE_2Si_2O_7$ multiphase silicates by component design with RE doping. *J Adv Ceram* 2024, **13**: 842–60.
[30] Tian Z, Ren X, Lei Y, *et al.* Corrosion of $RE_2Si_2O_7$ (RE=Y, Yb, and Lu) environmental barrier coating materials by molten calcium-magnesium-alumino-silicate glass at high temperatures. *J Eur Ceram Soc* 2019, **39**: 4245–54.
[31] Luo Y, Sun L, Wang J, *et al.* Phase formation capability and compositional design of *β*-phase multiple rare-earth principal component disilicates. *Nat Commun* 2023, **14**: 1275.
[32] Fan Y, Bai Y, Li Q, *et al.* Compositional design and phase formation capability of high-entropy rare-earth disilicates from machine learning and decision fusion. *Npj Comput Mater* 2024, **10**: 95.
[33] Meng H, Bai H, Wei P, *et al.* Data-driven phase prediction for polymorphic high-entropy rare-earth disilicates. *J Am Ceram Soc* 2025: e70248.
[34] Sun L, Luo Y, Ren X, *et al.* A multicomponent *γ*-type $(Gd_{1/6}Tb_{1/6}Dy_{1/6}Tm_{1/6}Yb_{1/6}Lu_{1/6})_2Si_2O_7$ disilicate with outstanding thermal stability. *Mater Res Lett* 2020, **8**: 424–30.
[35] Chen Z, Lin C, Zheng W, *et al.* Influence of average radii of RE^{3+} ions on phase structures and thermal expansion coefficients of high-entropy pyrosilicates. *J Adv Ceram* 2023, **12**: 1090–104.
[36] Fan Y, Bai Y, He X, *et al.* Revealing corrosion mechanisms and enabling predictive lifetime assessment of high-entropy rare-earth disilicates with superior CMAS corrosion resistance. *J Adv Ceram* 2026, **15**: 9221251.
[37] Liu Y, Zhuang L, Xie P, *et al.* $(Gd_{1/7}Dy_{1/7}Ho_{1/7}Er_{1/7}Tm_{1/7}Yb_{1/7}Lu_{1/7})_2Si_2O_7$ high-entropy disilicate: A promising environmental barrier coating material. *Sci China Mater* 2024, **67**: 2694–9.
[38] Wang X, Meng M, Xu F, *et al.* $(Lu_{1/7}Yb_{1/7}Sc_{1/7}Er_{1/7}Y_{1/7}Ho_{1/7}Dy_{1/7})_2Si_2O_7$ high entropy rare-earth disilicate with low thermal conductivity and excellent resistance to CMAS corrosion. *J Adv Ceram* 2024, **13**: 549–60.
[39] Zhang Z, Park Y, Park H, *et al.* Thermal cycle test performances of environmental barrier coatings of HfO_2-SiO_2/$Yb_2Si_2O_7$ in the steam environment at 1475 °C. *J Eur Ceram Soc* 2023, **43**: 5004–13.
[40] Zhang T, Wang Z, Wang Z, *et al.* Water vapor corrosion resistance of a novel environmental barrier coating candidate $(Yb_{0.2}Y_{0.2}Lu_{0.2}Er_{0.2}Sc_{0.2})_2Si_2O_7$. *Surf Coat Tech* 2025, **500**: 131907.
[41] Fan D, Zhong X, Zhang Z, *et al.* Investigation on behavior and mechanism of enhanced water vapor corrosion resistance for $(Lu_{0.25}Yb_{0.25}Er_{0.25}Y_{0.25})_2SiO_5$ environmental barrier coating. *J Eur Ceram Soc* 2023, **43**: 3737–45.
[42] Wang X, Xu F, Meng M, *et al.* A new high entropy rare earth disilicate ceramic $(Lu_{1/8}Yb_{1/8}Sc_{1/8}Er_{1/8}Y_{1/8}Ho_{1/8}Dy_{1/8}Tb_{1/8})_2Si_2O_7$: High temperature corrosion of water vapor and molten calcium–magnesium–aluminosilicate (CMAS). *J Alloy Compd* 2024, **983**: 173687.
[43] Dong Y, Ren K, Lu Y, *et al.* High-entropy environmental barrier coating for the ceramic matrix composites. *J Eur Ceram Soc* 2019, **39**: 2574–9.
[44] Liu Y, Liu Y, Zhuang L, *et al.* Composition-driven superior CMAS corrosion resistance of high-entropy rare-earth disilicates. *Corro Sci* 2024, **233**: 112108.
[45] Li K, Wang W, Liu W, *et al.* Effect of heterogeneous phases on thermal-mechanical properties and CMAS corrosion resistance of $(Sc_{0.33}Er_{0.33}Yb_{0.34})_2Si_2O_7$ ceramics. *J Eur Ceram Soc* 2025, **45**: 116847.
[46] Hu S, Zhong X, Wu Y, *et al.* Improving CMAS corrosion resistance of $RE_2Si_2O_7$ by non-equimolar component design. *Corro Sci* 2025, **257**: 113365.
[47] Sun L, Ren X, Luo Y, *et al.* Exploration of the mechanism of enhanced CMAS corrosion resistance at 1500 °C for multicomponent $(Er_{0.25}Tm_{0.25}Yb_{0.25}Lu_{0.25})_2Si_2O_7$ disilicate. *Corro Sci* 2022, **203**: 110343.
[48] Sun L, Luo Y, Tian Z, *et al.* High temperature corrosion of $(Er_{0.25}Tm_{0.25}Yb_{0.25}Lu_{0.25})_2Si_2O_7$ environmental barrier coating material subjected to water vapor and molten calcium–magnesium–aluminosilicate (CMAS). *Corro Sci* 2020, **175**: 108881.
[49] Guo L, Zhang B, Gao Y, *et al.* Interaction laws of RE_2O_3 and CMAS and rare earth selection criterions for RE-containing thermal barrier coatings against CMAS attack. *Corro Sci* 2024, **226**: 111689.
[50] Jiao Z, Xiao G, Wang C, *et al.* Tuning structure and CMAS corrosion behavior in high-entropy RE disilicate via average RE^{3+} ionic radius. *Corro Sci* 2025, **257**: 113280.
[51] Lin G, Wang Y, Yang L, *et al.* CMAS corrosion behavior of a novel high entropy $(Nd_{0.2}Gd_{0.2}Y_{0.2}Er_{0.2}Yb_{0.2})_2Zr_2O_7$ thermal barrier coating materials. *Corro Sci* 2023, **224**: 111529.

[52] Tu T, Liu J, Zhou L, *et al.* Graceful behavior during CMAS corrosion of a high-entropy rare-earth zirconate for thermal barrier coating material. *J Eur Ceram Soc* 2022, **42**: 649–57.
[53] Wei P, Bai H, Liu Y, *et al.* Improved CMAS corrosion resistance of high-entropy rare-earth monosilicates by multicomponent synergistic effects. *Ceram Int* 2025, **51**: 32175–83.
[54] Bai H, Wei P, Zhuang L, *et al.* Inverse design of high-entropy rare-earth monosilicates with superior CMAS corrosion resistance. *J Materiomics* 2026, **12**: 101123.
[55] Zou L, Cheng Y, Meng S, *et al.* Construction of a molten CMAS-resistant bilayer-structured apatite layer used for thermal barrier coatings. *J Adv Ceram* 2025, **14**: 9221173.
[56] Meng S, Guo L, Guo H, *et al.* CMAS-phobic and infiltration-inhibiting protective layer material for thermal barrier coatings. *J Adv Ceram* 2024, **13**: 1254–67.
[57] Wei F, Zhang D, Gong X, *et al.* A systematic analysis of the calcium-magnesium-aluminosilicate corrosion behavior of high-entropy $(5RE_{0.2})_2Si_2O_7$ materials. *Corro Sci* 2023, **219**.
[58] Dong Y, Ren K, Wang Q, *et al.* Interaction of multicomponent disilicate $(Yb_{0.2}Y_{0.2}Lu_{0.2}Sc_{0.2}Gd_{0.2})_2Si_2O_7$ with molten calcia-magnesia-aluminosilicate. *J Adv Ceram* 2022, **11**: 66–74.
[59] Turcer LR, Padture NP. Rare-earth pyrosilicate solid-solution environmental-barrier coating ceramics for resistance against attack by molten calcia–magnesia–aluminosilicate (CMAS) glass. *J Mater Res* 2020, **35**: 2373–84.
[60] Chen Z, Lin C, Zheng W, *et al.* Investigation on improving corrosion resistance of rare earth pyrosilicates by high-entropy design with RE-doping. *Corro Sci* 2022, **199**: 110217.
[61] Ridley MJ, Tomko KQ, Tomko JA, *et al.* Tailoring thermal and chemical properties of a multi-component environmental barrier coating candidate $(Sc_{0.2}Nd_{0.2}Er_{0.2}Yb_{0.2}Lu_{0.2})_2Si_2O_7$. *Materialia* 2022, **26**: 101557.
[62] Zhang Z, Xue Z, Wang H, *et al.* Corrosion behavior of $Y_xYb_{(2-x)}Si_2O_7$ environmental barrier coating materials against molten calcium-magnesium-aluminosilicate (CMAS) at 1475 °C. *Corro Sci* 2024, **227**.
[63] Wang X, Cheng M, Xiao G, *et al.* Preparation and corrosion resistance of high-entropy disilicate $(Y_{0.25}Yb_{0.25}Er_{0.25}Sc_{0.25})_2Si_2O_7$ ceramics. *Corro Sci* 2021, **192**.
[64] Abrar S, Ma Z, Liu L, *et al.* Excellent CMAS resistance of a newly developed equiatomic high entropy $(Dy_{1/4}Ho_{1/4}Tm_{1/4}Yb_{1/4})_2Si_2O_7$ ceramic pyrosilicate. *Ceram Int* 2023, **49**: 19840–50.
[65] Qian B, Wang Y, Zu J, *et al.* A review on multicomponent rare earth silicate environmental barrier coatings. *J Mater Res Technol* 2024, **29**: 1231–43.
[66] Chen Z, Lai X, Liang Y, *et al.* Progress in the degradation of thermal and environmental barrier coating materials caused by calcium-magnesium-aluminum-silicate deposit. *Extreme Materials* 2025, **1**: 9–37.
[67] Poerschke DL, Shaw JH, Verma N, *et al.* Interaction of yttrium disilicate environmental barrier coatings with calcium-magnesium-iron alumino-silicate melts. *Acta Mater* 2018, **145**: 451–61.
[68] Li J, Sun L, Du T, *et al.* High temperature interaction of $Y_4Al_2O_9/Y_2O_3$ under CMAS exposure: Mechanism of outstanding corrosion resistance through composition design to accelerate reaction-induced CMAS consumption. *J Adv Ceram* 2025, **14**: 9221106.
[69] Heuer AH, Lou VLK. Volatility diagrams for silica, silicon nitride, and silicon carbide and their application to high-temperature decomposition and oxidation. *J Am Ceram Soc* 1990, **73**: 2789–803.
[70] Krämer S, Yang J, Levi CG, *et al.* Thermochemical interaction of thermal barrier coatings with molten CaO–MgO–Al_2O_3–SiO_2 (CMAS) Deposits. *J Am Ceram Soc* 2006, **89**: 3167–75.
[71] Zhang Z, Sun J, Liu G, *et al.* High toughness and CMAS resistance of $REAlO_3/RE_2Zr_2O_7$ (RE=La, Nd, Sm, Eu, Gd, and Dy) composites with eutectic composition for thermal barrier coatings. *J Adv Ceram* 2024, **13**: 800–9.
[72] Chen L, Li B, Feng J. Rare-earth tantalates for next-generation thermal barrier coatings. *Prog Mater Sci* 2024, **144**: 101265.
[73] Majee BP, Bryce K, Huang L, *et al.* A high-entropy rare-earth phosphate and its principle single component $REPO_4$ for environmental barrier coatings. *J Adv Ceram* 2025, **14**: 9221041.
[74] Bryce K, Majee BP, Huang L, *et al.* A systematic study of thermomechanical properties and calcium–magnesium–aluminosilicate (CMAS) corrosion of multicomponent rare-earth phosphates. *J Adv Ceram* 2024, **13**: 1807–22.
[75] Zhang G, Shi J, Zhang J, *et al.* Investigation on crystallization behavior between $(Sc_xYb_{1-x})O_{1.5}$ and CMAS: A new insight in the effect of Sc substitution. *J Adv Ceram* 2024, **13**: 789–99.
[76] Mouret T, Maillé L, Danet J, *et al.* Thermochemical interaction of pure rare earth silicates (Y and Yb) with CMAS: Role and stability of the corrosion products. *Corro Sci* 2025, **250**: 112864.
[77] Okawa A, Nguyen ST, Nakayama T, *et al.* High-temperature corrosion of sintered $RE_2Si_2O_7$ (RE = Yb and Ho) environmental barrier coating materials by volcanic ash. *Int J Miner Metall Mater* 2024, **31**: 1628–38.
[78] Kim SH, Kim BN, Nagashima N, *et al.* High-temperature corrosion of spark plasma sintered Gd_2SiO_5 with volcanic ash for environmental barrier coatings. *J Eur Ceram Soc* 2021, **41**: 3161–6.

[79] Chen Z, Tian Z, Zheng L, *et al.* $(Ho_{0.25}Lu_{0.25}Yb_{0.25}Eu_{0.25})_2SiO_5$ high-entropy ceramic with low thermal conductivity, tunable thermal expansion coefficient, and excellent resistance to CMAS corrosion. *J Adv Ceram* 2022, **11**: 1279–93.
[80] Tian Z, Ming K, Zheng L, *et al. In-situ* observation and mechanism of calcium–magnesium–alumina–silicate (CMAS) melts-induced degradation of RE_2SiO_5 (RE = Tb, Dy, Ho, Y, Er, Tm, and Yb) ceramics at 1500 °C. *J Adv Ceramics* 2023, **12**: 2315–30.
[81] Xiao G, Shen Q, Tian Y, *et al.* Investigation on the relation of microstructures and CMAS corrosion resistance of high entropy RE disilicates. *Corro Sci* 2024, **227**: 111727.
[82] Perrudin F, Rio C, Vidal-Sétif MH, *et al.* Gadolinium oxide solubility in molten silicate: dissolution mechanism and stability of $Ca_2Gd_8(SiO_4)_6O_2$ and $Ca_3Gd_2(Si_3O_9)_2$ silicate phases. *J Eur Ceram Soc* 2017, **37**: 2657–65.
[83] Perrudin F, Vidal-Sétif MH, Rio C, *et al.* Influence of rare earth oxides on kinetics and reaction mechanisms in CMAS silicate melts. *J Eur Ceram Soc* 2019, **39**: 4223–32.
[84] Li J, Zhou C, Wang J, *et al.* Exploration on intrinsic corrosion resistance of β-$Lu_2Si_2O_7$ against calcium–magnesium–aluminosilicate (CMAS) at 1500 °C via grain boundary engineering. *Mater Design* 2025, **253**: 113965.
[85] Pujol G, Ansart F, Bonino JP, *et al.* Step-by-step investigation of degradation mechanisms induced by CMAS attack on YSZ materials for TBC applications. *Surf Coat Tech* 2013, **237**: 71–8.
[86] Shan X, Chen W, Yang L, *et al.* Pore filling behavior of air plasma spray thermal barrier coatings under CMAS attack. *Corro Sci* 2020, **167**: 108478.
[87] Gao X, Wang Z, Luo Y, *et al.* Multicomponent $(Gd_{x1}Ho_{x2}Yb_{x3}Lu_{x4})_2Si_2O_7$ disilicates: compositional modulation and CMAS corrosion resistance at 1300°C. *J Am Ceram Soc* 2026, **109**: e70533.
[88] Summers WD, Poerschke DL, Park D, *et al.* Roles of composition and temperature in silicate deposit-induced recession of yttrium disilicate. *Acta Mater* 2018, **160**: 34–46.
[89] Chen Z, Wang Y, Huang Y, *et al.* Investigation on improving the comprehensive performance of environmental barrier coating materials by high-entropy multiphase design. *Npj Mat Degrad* 2024, **8**: 37.
[90] Costa G, Harder BJ, Bansal NP, *et al.* Thermochemistry of calcium rare-earth silicate oxyapatites. *J Am Ceram Soc* 2020, **103**: 1446–53.
[91] Duffy JA, Ingram MD. An interpretation of glass chemistry in terms of the optical basicity concept. *J Non-Cryst Solids* 1976, **21**: 373–410.
[92] Zhao X, Wang X, Lin H, *et al.* Electronic polarizability and optical basicity of lanthanide oxides. *Physica B:* 2007, **392**: 132–6.